Further explorations of Skyrme-Hartree-Fock-Bogoliubov mass formulas. V. Extension to fission barriers

M. Samyn and S. Goriely*

Institut d'Astronomie et d'Astrophysique, ULB-CP226, B-1050 Brussels, Belgium

J. M. Pearson

Département de Physique, Université de Montréal, Montréal, Québec H3C 3J7, Canada

Large-scale fission barrier calculations have been performed in the framework of the Skyrme-Hartree-Fock model. Our Hartree-Fock-Bogoliubov calculations restore broken symmetries such as translational invariance, particle-number conservation, parity, and, in a more approximate way, rotational invariance. Axial symmetry is imposed, but reflection asymmetry is allowed. The energy surface properties are analyzed with the flooding method. A large set of Skyrme interactions, which were fitted to all known masses under different specific constraints, is used to study the main effects influencing the energy surface and the barrier heights. The principal interaction used in the comparison with experimental barriers is BSk8, the force on which the HFB-8 mass table is based. We found that for nuclei with $92 \leqslant Z \leqslant 98$ the agreement of our calculations with experimental data is excellent; the rms deviation on the primary barriers is 0.722 MeV. For lighter nuclei, however, the calculated primary barriers are always too high because of the existence of a third barrier at very high deformations. However, our calculated superheavy barriers appear to be too low, although they are consistent with previous calculations.

I. INTRODUCTION

The *r*-process of stellar nucleosynthesis is known to depend on the masses and fission barriers (among other quantities) of nuclei that are so neutron rich that there is no hope of being able to measure them in the laboratory. (See Refs. [1,2] for reviews discussing the nuclear data required for an understanding of the *r*-process.) It is thus of the greatest importance to be able to make reliable extrapolations of these quantities away from the known region, relatively close to the stability line, out toward the neutron drip line. In an attempt to put the extrapolations on as rigorous a footing as possible we are following a Hartree-Fock-Bogoliubov (HFB) approach using Skyrme forces and a δ-function pairing force, with blocking included, as described in Ref. [3]. As far as nuclear masses are concerned we have already made considerable progress along these lines, developing a number of HFB mass models, labeled HFB-1 to HFB-9 [3–8] (with corresponding sets of force parameters labeled BSk1 to BSk9, respectively). The first of these [3] was fitted to essentially all the mass data of the 1995 Atomic Mass Evaluation (AME) [9] but was not satisfactory in its predictions of new data. However, all the later models, HFB-2 to HFB-9, reproduce the masses of the 2149 measured nuclei with $Z, N \geqslant 8$ given in the 2003 AME [10] with an rms error smaller than 0.7 MeV, except for HFB-9 (see the last line of Table I).

In the present paper we investigate the feasibility of extending our HFB project to the calculation of fission barriers by calculating the barriers of a large fraction of nuclei for which we have found data. We have also calculated the barriers of just a few highly neutron-rich nuclei to form some idea of how our extrapolations will compare with those of other models, although we leave to a later paper the calculation of the barriers of all the nuclei involved in the *r*-process. There have, of course, already been many self-consistent mean-field calculations of the barriers of some particular nuclei: Two recent ones are [11] and [12], the latter giving an extensive list of earlier calculations. However, the work we describe here is the first in which one attempts to see how well a force that has been fitted to essentially all the mass data with the HFB method can work for the calculation of fission barriers, and inversely what the fission-barrier calculations can teach us about forces designed to predict masses.

Concerning our ultimate objective of making HFB calculations of all the barriers involved in the *r*-process, it should be noted that at the present time there are only two systematic compilations of barrier calculations covering all the required nuclei. The first is the 1980 macroscopic-microscopic (mic-mac) calculation of Howard and Möller [13], but new calculations of Möller *et al.* [14] using the finite-range liquid-drop model (FRLDM) with the Tondeur flooding algorithm [15] cast doubt on all previous mic-mac calculations of barriers. The only other compilation is the much more (but not completely) microscopic calculation of Mamdouh *et al.* [16], which is based on the ETFSI (extended Thomas-Fermi plus Strutinsky integral) high-speed approximation to the Skyrme-HF method, with pairing handled in the BCS approximation. This method was originally developed as a mass model [17–20] and led to the construction of the ETFSI-1 mass table [21]. The extension of the ETFSI method to the calculation of fission barriers was first described in Ref. [15], with results being shown

___

*Electronic address: sgoriely@astro.ulb.ac.be

for all barriers that had been measured. In the extrapolation toward highly neutron rich nuclei some striking differences are found between the Howard-Möller predictions [13] and those of Mamdouh *et al.* [16], especially in the vicinity of the $N = 184$ magic number. (We should also mention the calculations of Myers and Swiatecki [22], based on zeroth-order Thomas-Fermi calculations [23]. Actually, Ref. [22] gives just a formula representing the main trends of Thomas-Fermi barrier calculations, although a prescription is given in Ref. [22] for adding shell corrections, as done in Ref. [16]. Generally speaking, the barriers of Myers and Swiatecki [22] lie much closer to the Howard-Möller predictions than to those of the ETFSI method [16].)

It will be seen that we are now retracing with the HFB method essentially the same route that was followed with the ETFSI method, with the present paper corresponding to Ref. [15]. Section II is a résumé of the HFB framework as we use it here and in our latest mass models. In particular, we describe our method for constructing the multidimensional energy surface and extracting its main characteristics, namely, the minima and saddle points. In Sec. III we discuss some preliminary calculations performed with a view to facilitating the interpretation of the general results presented in Sec. IV. We begin this latter section by explaining why we regard the force BSk8 as the one best adapted to the calculation of barriers, after which we present our extensive results obtained with this force and make a detailed comparison with experimental data. In Sec. V we then compare the barrier predictions of the different force models, with a view both to an understanding of the present results and toward future improvements. This is followed (Sec. VI) by a brief discussion of the barriers of highly neutron rich nuclei. Our conclusions are drawn in Sec. VII.

II. THE FRAMEWORK

A. Parametrization of the models

In all our HFB models, described in [3] and [7], the Skyrme force acting in the particle-hole channel has the conventional 10-parameter form

$$v_{ij} = t_0(1+x_0 P_\sigma)\delta(\mathbf{r}_{ij}) + t_1(1+x_1 P_\sigma)\frac{1}{2\hbar^2}\{p_{ij}^2\delta(\mathbf{r}_{ij}) + \text{h.c.}\}$$
$$+ t_2(1+x_2 P_\sigma)\frac{1}{\hbar^2}\mathbf{p}_{ij}\cdot\delta(\mathbf{r}_{ij})\mathbf{p}_{ij} + \frac{1}{6}t_3(1+x_3 P_\sigma)\rho^\gamma\delta(\mathbf{r}_{ij})$$
$$+ \frac{i}{\hbar^2}W_0(\boldsymbol{\sigma}_i + \boldsymbol{\sigma}_j)\cdot\mathbf{p}_{ij}\times\delta(\mathbf{r}_{ij})\mathbf{p}_{ij}. \quad (1)$$

The δ-function pairing force acting in the particle-particle channel is allowed to have a density dependence; thus

$$v_{\text{pair}}(\mathbf{r}_{ij}) = V_{\pi q}\left[1 - \eta\left(\frac{\rho}{\rho_0}\right)^\alpha\right]\delta(\mathbf{r}_{ij}), \quad (2)$$

where $\rho \equiv \rho(\mathbf{r})$ is the local density, and ρ_0 is its equilibrium value in symmetric infinite nuclear matter (INM). Actually, most of our HFB models have η set equal to zero (i.e., have density-independent pairing). (The case $\eta = 1$ corresponds to the pairing effectively vanishing at the center of the

nucleus and is somewhat misleadingly referred to as "surface pairing.")

An essential aspect relating to a δ-function pairing force concerns the cutoff to be applied to the space of single-particle (sp) states over which the force is allowed to act. For HFB-1 the sp spectrum was cut off above an energy of $\hbar\omega$, but it was found [4] that it was this simplistic choice that was in large part responsible for the major disagreement of HFB-1 with the post-1995 data. In all subsequent models the sp spectrum is confined to lie in the range

$$\varepsilon_F - \varepsilon_\Lambda \leqslant \varepsilon_i \leqslant \varepsilon_F + \varepsilon_\Lambda, \quad (3)$$

where ε_F is the Fermi energy of the nucleus in question and ε_Λ is a free parameter.

A special feature of our pairing is that we allow the pairing-strength parameter $V_{\pi q}$ to be different for neutrons and protons and also to depend on whether we have an odd number of nucleons ($V_{\pi q}^-$) or an even number ($V_{\pi q}^+$) (i.e., the neutron pairing strength, for example, depends on whether N is even or odd). We refer to this last feature as "staggered pairing," and to understand much of the later discussion of our fission results we now recall our reasons for introducing it.

If the pairing force is fitted directly to even-odd mass differences then both even and odd open-shell spherical nuclei tend to be badly underbound. The most obvious origin of this deficiency is our failure to go beyond the mean-field approximation and take explicit account of quadrupole correlations, as treated recently by Bender *et al.* [24]. Actually, insofar as we include a rotational correction (see the following), we do take rough account of these correlations in deformed nuclei, but we neglect completely the vibrational mode, the almost equally striking manifestation of quadrupole correlations in spherical nuclei. In any case, we fit the pairing force not to the even-odd mass differences but to the absolute masses, with the result that our pairing force is considerably stronger than it would be otherwise, being required to represent not only the true pairing correlations but also the quadrupole (and possibly other) correlations. If now our pairing force had the same coupling constants in even and odd nuclei then the even-odd mass differences would be too strong. Thus by allowing for the possibility of staggered pairing optimal mass fits will inevitably have stronger pairing coupling constants in odd nuclei than in even nuclei. However, even if we had taken quadrupole correlations correctly into account, it is possible that a staggered pairing would still have emerged from the mass fits, for reasons connected with time-reversal invariance, as discussed in Sec. II C.

To take account of a quite different deviation from the mean-field picture, all our HFB models except HFB-1 add to the total energy corresponding to the aforementioned force a phenomenological Wigner term of the form

$$E_W = V_W \exp\left\{-\lambda\left(\frac{N-Z}{A}\right)^2\right\} + V_W'|N-Z|\exp\left\{-\left(\frac{A}{A_0}\right)^2\right\}; \quad (4)$$

a somewhat simpler form was used in HFB-1; see Ref. [4] for a discussion concerning the microscopic origin of the two terms. Since $N \gg Z$ for all the nuclei considered in this

TABLE I. Parameters of BSk and SLy6 [25] forces; the last line shows the rms deviation with respect to the 2149 nuclei with $Z, N \geqslant 8$ given in the 2003 AME [10] (not available for SLy6).

	BSk1	BSk2	BSk6	BSk7	BSk8	BSk9	SLy6$^{(\delta, \delta\rho)}$
t_0 (MeV fm^3)	−1830.4515	−1790.6248	−2043.3174	−2044.2484	−2035.5245	−2043.0994	−2479.5000
t_1 (MeV fm^5)	262.9704	260.9963	382.1273	385.9730	398.8208	406.5746	462.1800
t_2 (MeV fm^5)	−296.4463	−147.1672	−173.8785	−131.5248	−196.0032	−195.7471	−448.6100
t_3 (MeV fm$^{3(1+\gamma)}$)	13444.69	13215.09	12511.66	12518.75	12433.36	12490.95	13673.00
x_0	0.599988	0.498986	0.735859	0.729193	0.773828	0.521846	0.825000
x_1	−0.500000	−0.089752	−0.799153	−0.932336	−0.822006	−0.880337	−0.465000
x_2	−0.500000	0.224411	−0.358983	−0.050127	−0.389640	−0.358806	−1.000000
x_3	0.823074	0.515675	1.234779	1.236280^a	1.309331	0.891955	1.355000
W_0 (MeV fm^5)	117.971	119.047	142.380	146.930	147.810	146.097	122.000
γ	1/3	0.34329	1/4	1/4	1/4	1/4	1/6
$V_{\pi n}^+$ (MeV fm^3)	−227.000	−237.602	−321.213	−505.135	−314.015	−311.798	(−307.5, −1250)
$V_{\pi n}^-$ (MeV fm^3)	−236.000	−246.905	−337.928	−531.344	−329.780	−328.102	(−307.5, −1250)
$V_{\pi p}^+$ (MeV fm^3)	−251.000	−265.263	−324.541	−514.207	−293.019	−288.464	(−320.0, −1250)
$V_{\pi p}^-$ (MeV fm^3)	−260.000	−277.768	−342.410	−541.104	−309.924	−304.608	(−320.0, −1250)
η	0	0	0	0.45	0	0	(0, 1)
α	0	0	0	0.47	0	0	(0, 1)
cutoff (MeV)	$<\hbar\omega$	$\epsilon_F \pm 15$	$\epsilon_F \pm 17$	$\epsilon_F \pm 17$	$\epsilon_F \pm 17$	$\epsilon_F \pm 16.5$	$\epsilon_F + 5$
Σ (MeV)	0.796	0.659	0.666	0.657	0.635	0.733	NA^b

^{a}This value was misprinted in Ref. [6]; we thank J. Rikovska Stone for pointing this out to us.
^{b}NA = not available.

paper (see Table IV), the first Wigner term will obviously be irrelevant here. But for the same reason the second term, with its $|N - Z|$ factor, could in principle become significant for fission, as indeed it is in the work of Möller *et al.* [14]. However, the Wigner term used by this latter group contains no $\exp\{-(A/A_0)^2\}$ factor, whereas in our own mass fits we always find $A_0 \leqslant 30$, which means that this term, like the first, has no role to play in our barrier calculations. Even if a Wigner term with an $|N - Z|$ factor would lead to an improved agreement with measured barriers (provided it is given an appropriate deformation dependence), there is no independent evidence for the existence of such a term in the heavy nuclei of interest here, and the mass data point rather to its nonexistence.

The sets of the parameters appearing in Eqs. (1)–(4) for the different models HFB-1, HFB-2, and HFB-6 to HFB-9 are given in Table I, along with the corresponding rms errors, as explained in Sec. I. (The omitted models HFB-3 to HFB-5 are intermediate cases of no intrinsic interest in the present study.) Since we will compare some of our predictions for these forces with those made for the SLy6 force [25], Table I shows also the parameters of this last force, with two different prescriptions of the pairing force that have been proposed, namely a density-independent version (SLy6$^\delta$) and a density-dependent version (SLy6$^{\delta\rho}$) [see Eq. (2)]; the pairing parameters for SLy6 come from Bender [26].

The corresponding macroscopic parameters (infinite and semi-infinite nuclear matter) are given in Table II. In this table

TABLE II. Properties of (semi-)infinite nuclear matter for the forces presented in Table I. We also show the corresponding effective surface coefficient of ^{240}Pu and the neutron-skin thickness of ^{208}Pb.

	BSk1	BSk2	BSk6	BSk7	BSk8	BSk9	SLy6
M_s^*/M	1.05	1.04	0.80	0.80	0.80	0.80	0.69
M_v^*/M	1.05	0.86	0.86	0.87	0.87	0.89	0.80
a_v (MeV)	−15.805	−15.794	−15.749	−15.760	−15.824	−15.915	−15.920
ρ_0 (fm^{-3})	0.1573	0.1575	0.1575	0.1575	0.1589	0.1589	0.1589
ρ_{frmg}/ρ_0	1.44	1.13	1.82	1.62	1.70	1.45	4.30
J (MeV)	27.81	28.00	28.00	28.00	28.00	30.00	31.96
K_v (MeV)	231.228	233.573	229.064	229.187	230.298	231.314	229.848
L (MeV)	7.197	7.996	16.858	17.992	14.860	39.880	47.447
a_{sf}^0 (MeV)	17.54	17.46	17.18	17.29	17.64	17.92	17.74
Q (MeV)	45.7	45.8	44.8	45.3	45.5	35.5	33.3
a_{ss} (MeV)	−37.0	−37.3	−36.9	−36.2	−36.5	−50.9	−61.7
a_{sf} (^{240}Pu) (MeV)	15.8	15.7	15.4	15.6	15.9	15.5	14.8
θ_n (^{208}Pb) (fm)	0.11	0.12	0.12	0.12	0.12	0.15	0.16

M_s^*/M and M_v^*/M are the isoscalar and isovector effective masses, respectively, a_v is the equilibrium energy per nucleon of symmetric INM, and ρ_0 is the corresponding density, as previously defined. Also ρ_{frmg} is the density at which neutron matter flips over into a ferromagnetic state that has no energy minimum and would collapse indefinitely [27], J is the symmetry coefficient [28], K_v is the incompressibility of symmetric INM [28], and L is the density-symmetry coefficient [28]. All the foregoing coefficients refer to INM, but the next two lines of Table II refer to semi-infinite nuclear matter (SINM): a_{sf}^0 and Q are the usual surface coefficient and surface-stiffness coefficient, respectively [28]. (See Appendix A for the extraction of Q from calculations of SINM.) We also show the so-called surface-symmetry coefficient [28]

$$a_{ss} = \frac{2L}{K_v} a_{sf}^0 - 9\frac{J^2}{4Q}, \tag{5}$$

which, according to the droplet model [28], gives the effective surface coefficient of a nucleus with relative neutron excess $I = (N - Z)/A$ as

$$a_{sf}(I) = a_{sf}^0 + a_{ss} I^2; \tag{6}$$

this quantity is involved directly in the fissility parameter,

$$x = \frac{a_{\mathrm{coul}} Z^2}{2 a_{sf}(I) A}, \tag{7}$$

where $a_{\mathrm{coul}} = 3e^2/5r_0$. For convenience the penultimate line of Table II shows the value of $a_{sf}(I)$ for ^{240}Pu. Finally, Table II also gives the neutron-skin thickness $\theta_n = R_n - R_p$ for ^{208}Pb, where R_n and R_p are the rms radii of the neutron distribution and point-proton distribution, respectively.

B. The oscillator basis

As described in Ref. [3], the HFB wave function is expanded in the basis defined by a deformed oscillator potential,

$$V(\eta, z) = \tfrac{1}{2} M \big(\omega_\perp^2 \eta^2 + \omega_z^2 z^2 \big), \tag{8}$$

where $\eta = (x^2 + y^2)^{1/2}$ [29]. We denote these basis functions by $\psi_\alpha(\eta, z, \phi, \sigma)$, where ϕ is the azimuthal angle and σ is the usual nucleon-spin variable; also $\alpha \equiv \{n_\eta, n_z, \Lambda\}$, where n_η and n_z represent the number of nodes in the η and z variables, respectively, and Λ is the eigenvalue of the projection on the z axis of the orbital angular momentum, L_z. The corresponding energy eigenvalue is $E_{\mathrm{osc}} = (2n_\eta + |\Lambda| + 1)\hbar\omega_\perp + (n_z + 1/2)\hbar\omega_z$.

This basis is truncated according to

$$E_{\mathrm{osc}} - E_{\mathrm{osc}}^0 \leqslant n_{\max}\hbar\bar{\omega}, \tag{9}$$

where $\bar{\omega} = (\omega_z \omega_\perp^2)^{1/3}$ and $E_{\mathrm{osc}}^0 = \hbar\omega_\perp + \hbar\omega_z/2$. The choice of values for ω_z and $\omega_\perp$ is discussed in Sec. II D. As for the number of shells (i.e., the value of the dimensionality $n_{\max}$) necessary to ensure sufficient convergence of the expansion, we show in Figs. 1 and 2 the results of extensive tests that we made on ^{240}Pu and ^{268}Po, respectively; the former is close to the stability line and the latter is close to the neutron drip line. The upper panel of each of these figures shows the total energy E_{tot}, calculated with the constrained (see Sec. II D) HFB + PLN method [7], for $17 \leqslant n_{\max} \leqslant 27$ and at five deformations
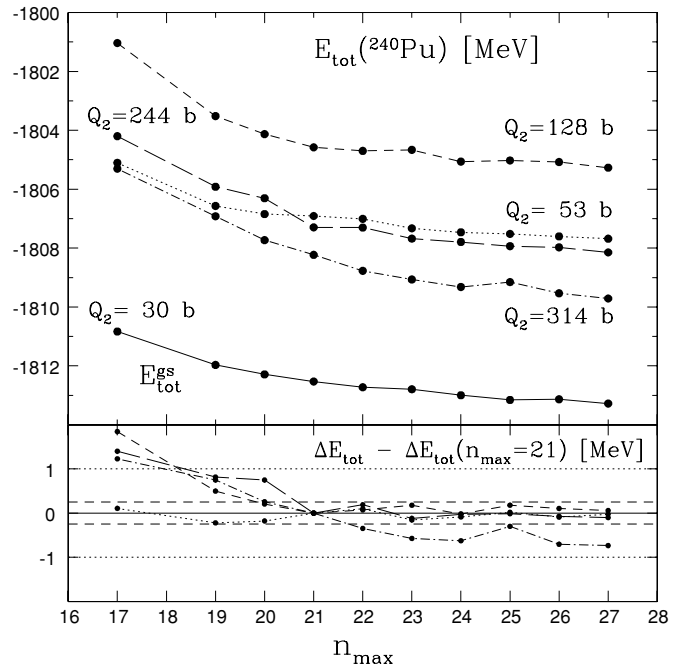
FIG. 1. Energy and deformation energy convergence for ^{240}Pu as function of dimensionality $n_{\max}$: (upper panel) total energy (constrained HFB + PLN) at five deformations; (lower panel) deformation energy $\Delta E_{\mathrm{tot}} = E_{\mathrm{tot}}(Q_2) - E_{\mathrm{tot}}^{\mathrm{gs}}$, normalized to $\Delta E_{\mathrm{tot}}(n_{\max} = 21)$ (see text).

typically encountered along the fission path, the lowest of which corresponds to the ground state [with an energy labeled $E_{\mathrm{tot}}^{\mathrm{gs}} = E_{\mathrm{tot}}(Q_2 \simeq 30)$b in the case of ^{240}Pu]. For each value of
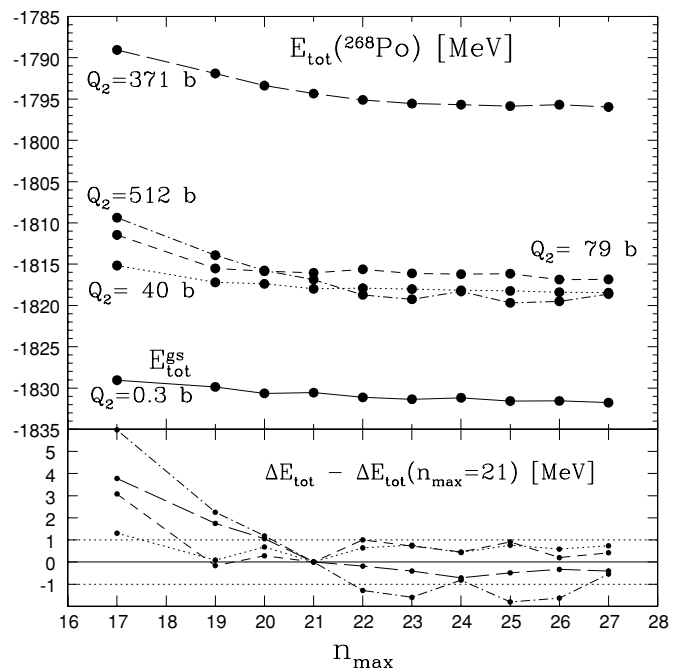
FIG. 2. Same as Fig. 1 for ^{268}Po, situated close to the neutron drip line. Note that the neutron Fermi energy becomes positive for $Q_2 \gtrsim 500$ b.

n_{max} we define a deformation energy $\Delta E_{tot}(Q_2) = E_{tot}(Q_2) - E_{tot}^{gs}$, and then plot $\Delta E_{tot}(n_{max}) - \Delta E_{tot}(n_{max} = 21)$ in the lower panels of the respective figures. We see that for all but the largest deformation in each case, by $n_{max} = 21$ the deformation energy has converged to within 0.2 MeV in the case of ^{240}Pu, and to within 1 MeV in the case of ^{268}Po, as indicated by the horizontal dashed lines. Since this amounts to no more than 5% of the barrier height in the case of ^{240}Pu (around 5 MeV) and 2.5% in the case of ^{268}Po (more than 40 MeV), we decided that it is sufficient to take $n_{max} = 21$.

It is well known that the outer barrier configuration is very often reflection asymmetric, as shown by fission-fragment mass distributions. Left-right asymmetry has therefore been included in the present study, but we do not take account of the possibility of triaxial deformations, since the correction that they introduce is generally much smaller than the possible correction arising from left-right asymmetry. Typically, triaxiality would reduce our calculated barrier heights by around 0.6 MeV [30].

C. Restoration of broken symmetries

Mean-field approaches, such as the HFB used here, establish an intrinsic frame of the nucleus and consequently break several symmetries of the Hamiltonian and the wave function in the laboratory frame [31,32]. In particular, all finite nuclei break translational invariance, the Bogoliubov treatment of pairing leads to particle-number nonconservation in all nuclei, all but even-even nuclei violate time-reversal invariance, deformed nuclei break rotational invariance, and reflection-asymmetric shapes break the parity symmetry. These symmetry breakings lead to the inclusion of many desirable correlations in the modeling (as multiparticle-multihole states), but at the same time they give rise to an admixture of excited states to the calculated ground state. The broken symmetries can be restored rigorously by projecting the wave function on the exact quantum numbers. A simpler procedure aims at estimating the contribution to the binding energy in a suitable approximation and adding the resulting correction to the binding energy. We adopted such a procedure in some of our previous mass formulas, in particular to estimate the center-of-mass (cm) correction from the recoil energy, and the rotational correction within the cranking model [33]. We now summarize the various approaches adopted in this paper.

1. Center-of-mass motion

As far as the cm correction is concerned, the approximate prescription of Butler *et al.* [34] was replaced in [6] by a more fundamental calculation of the recoil energy.

2. Particle-number projection

The particle-number symmetry has been very recently restored and taken into account in the global mass fit [7]. The projection of the wave function on the exact number of particles is performed after a variation that includes the approximate Lipkin-Nogami projection before variation (referred to as PLN).

3. Violation of time-reversal invariance

The presence of an odd neutron or proton (or both) leads to a violation of time-reversal invariance [35], and we make no explicit attempt to project out time-reversible states. The result will be a tendency for odd-*A* and odd-odd nuclei to be underbound, and it is possible that at least a part of the extra pairing strength in these nuclei that always emerges in our mass fits, made with the "staggered-pairing" degree of freedom, is actually compensating for the violation of time reversibility that our model has introduced. (Note that our HFB calculations incorporate blocking.)

4. Rotational correction

As in all our previous work we make a correction for the spurious rotational energy of deformed nuclei according to

$$E_{rot} = \frac{\langle \hat{J}^2 \rangle}{2\mathcal{I}}, \qquad (10)$$

where $\hat{J}$ is the angular momentum operator and $\mathcal{I}$ is the moment of inertia. The cranking model [36–38] gives this latter quantity as

$$\mathcal{I}_{cr} = 2 \sum_{k,k'>0} \frac{|\langle k|J_x|k'\rangle|^2}{E_k + E_{k'}} (u_k v_{k'} - u_{k'} v_k)^2, \qquad (11)$$

where the summation runs over quasiparticle sp states, the E_k are the corresponding quasiparticle energies, the matrix elements are calculated in the canonical basis, and $v_k^2 = 1 - u_k^2$ are the corresponding occupation probabilities.

As explained in detail in [7], the cranking model as such was not appropriate for our mass fits, and we therefore adopted a mixed prescription, combining linearly the rigid and cranking values of the moment of inertia. However, this prescription was found in [7] to strongly underestimate the isomeric-state energies, and to fit both these and the ground state a modified version of the cranking prescription was introduced in [7]:

$$\mathcal{I}_{crth} = \frac{1}{b} \mathcal{I}_{cr} \coth(c\beta_2), \qquad (12)$$

where $b = 0.65$ and $c = 4.5$ for HFB-8 (with corresponding figures for HFB-9 of 1.00 and 4.2 [8]). We found that this prescription is not only equivalent to the "mixed" prescription for ground states and likewise avoids any problems in the spherical limit but also leads to considerable improvements in the estimates for the shape isomers. For barrier calculations based on the BSk8 Skyrme interaction and compared to experimental data in Sec. IV, Eq. (12) is used in Eq. (10). In the calculations of Secs. III and V, where we investigate the dependence of barrier heights on various factors, we take the rigid value of the moment of inertia, this being sufficient for such purely comparative studies.

5. Parity-symmetry restoration

The role of parity projection (see Appendix B for the formalism) in the determination of the outer barrier of ^{240}Pu is shown in Fig. 3 as a function of the octupole degree of
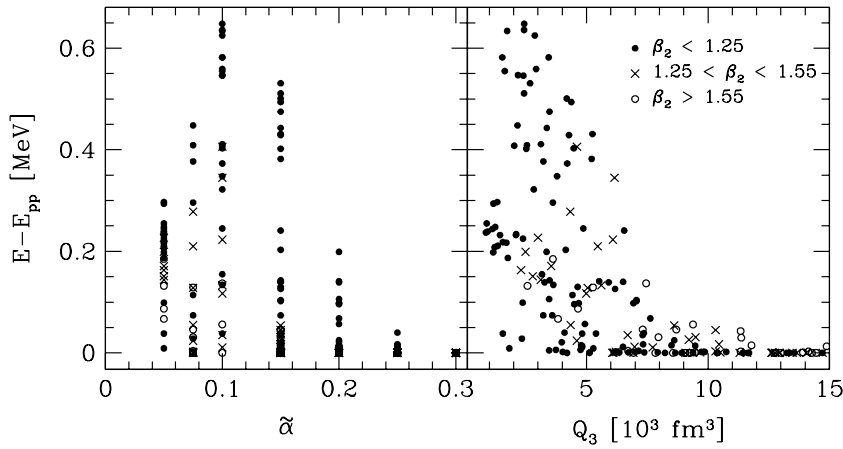
FIG. 3. Projection energy of the positive-parity state (unprojected energy − projected energy) as a function of the asymmetry parameter $\tilde{\alpha}$ (left panel) and of the octupole moment Q_3 (right panel), for part of the ^{240}Pu three-dimensional energy surface calculated with the HFBCS + PLN (BSk8) model: $1.55 \leqslant c \leqslant 1.80$ and $-0.20 \leqslant h \leqslant 0.15$.

freedom ($\tilde{\alpha}$ or Q_3). We have seen that the outer barrier height of ^{240}Pu (lowered by 3.7 MeV when the reflection symmetry is broken) is characterized by $Q_3 = 12,670$ fm^3. Therefore, Fig. 3 clearly shows that parity projection has no effect on the determination of that barrier height. However, it modifies the shape of the energy surface at smaller deformation (both β_2 and β_3) in a non-negligible way that may affect the fission path.

The situation is different for the ^{194}Pb nucleus, as shown in Fig. 4, where the impact of the parity projection is studied with Skyrme force MSk7 [39]. The octupole correlations of the superdeformed shape isomer of ^{194}Pb have already been studied in [40] with the SkM* Skyrme force. The evolution from the ground state up to the superdeformed isomeric state is shown as a function of the octupole moment for different

quadrupole moments, the asymmetric character of the minima as well as of the entire fission path appearing only after the projection has been applied: Without the parity projection, the ground state is reflection symmetric and the static path along the energy surface in the quadrupole-octupole deformation space is characterized by a reflection-symmetric shape. By adding the parity projection, the static path always favors the octupole degree of freedom. This result is in good agreement with the result obtained in [40] for the neighboring nucleus ^{192}Hg with the SkM* Skyrme force. In [40], the reflection-symmetric isomeric state becomes asymmetric when the wave function is projected on the good parity quantum number, with a lowering of 0.6 MeV at $(Q_2, Q_3) = (4200 \text{ fm}^2, 800 \text{ fm}^3)$; in a similar way, the isomeric state of ^{194}Pb is lowered by 0.5 MeV at $(Q_2, Q_3) = (4460) \text{ fm}^2, 760 \text{ fm}^3)$. We note that the lowering
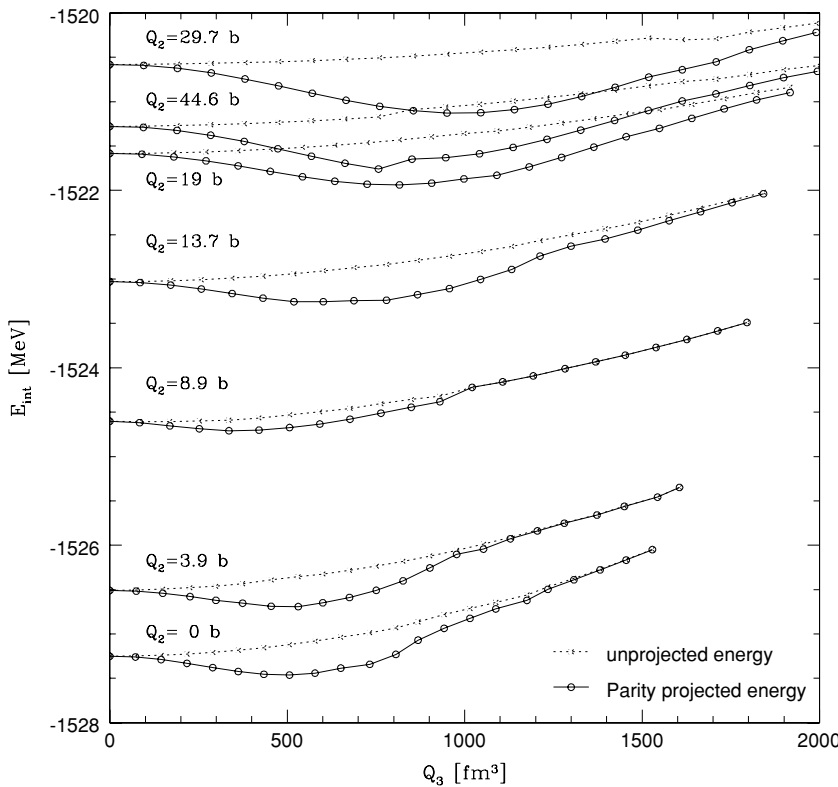
FIG. 4. Evolution [energy curves (in MeV) of ^{194}Pb] of the parity projection effect with respect to the octupole moment, at different quadrupole moments

of the ground-state energy by about 0.2 MeV increases the disagreement with the experimental data; with BSk8, this disagreement is reduced by 0.9 MeV, but the conclusion of the present analysis remains unchanged.

D. The energy surface and its analysis

The investigation of the fission process requires, among other things, a complete knowledge of the dependence of the nuclear energy with respect to as many spatial degrees of freedom as possible. In self-consistent calculations, where the only assumptions made on the nuclear-density distribution are the symmetries imposed, the number of degrees of freedom is not restricted by any nuclear-shape parametrization: The initial wave function converges to the nearest configuration that corresponds to a local energy minimum. This means that to obtain the multidimensional energy surface, the mean field must be constrained at every relevant deformation, with the deformation described by the initial wave function being as close as possible to its corresponding constrained value.

In the present HFB calculations we take for the constrained degrees of freedom the quadrupole, octupole, and hexadecapole moments, Q_2, Q_3, and Q_4, respectively, where

$$Q_l \equiv \langle \hat{Q}_l \rangle = \int \rho(\mathbf{r}) \hat{Q}_l d\mathbf{r}, \qquad (13)$$

in which we have introduced the operator

$$\hat{Q}_l = 2r^l P_l(\cos\theta). \qquad (14)$$

To constrain the HFB calculation to given values Q_{2c}, Q_{3c}, and Q_{4c} of Q_2, Q_3, and Q_4, respectively, we adopt the "quadratic constraint" variant of the constrained HF method, as introduced by Giraud et al. [41] and applied to fission by Flocard et al. [42]. Referring, for example, to Sec. 7.6 of Ring and Schuck [31], we make an unrestricted variation of the modified energy

$$\bar{E} = E + \tfrac{1}{2} c_q (Q_2 - Q_{2c})^2 + \tfrac{1}{2} c_o (Q_3 - Q_{3c})^2$$
$$+ \tfrac{1}{2} c_h (Q_4 - Q_{4c})^2, \qquad (15)$$

where $E = \langle H \rangle$, the expectation value of the unconstrained model Hamiltonian H, and c_q, c_o, and c_h are the somewhat arbitrary strength constants of the respective constraints. At the level of the HFB equations the effect of the constraints is simply to modify the usual mean field U, calculated at the end of each iteration, according to

$$U' = U + c_q (Q_2 - Q_{2c}) \hat{Q}_2 + c_o (Q_3 - Q_{3c}) \hat{Q}_3$$
$$+ c_h (Q_4 - Q_{4c}) \hat{Q}_4, \qquad (16)$$

where the current values of Q_2, Q_3, and Q_4 are to be taken as calculated at the end of the previous iteration. Of course, the final converged values of the Q_l will not be exactly equal to the imposed values Q_{lc}.

To construct the energy surface in the relevant region of deformation space we make extensive recourse to the ETFSI fission-barrier calculations [15,16]. For any given deformation these latter calculations began with an essentially macroscopic ETF calculation, followed by the determination of a shell

correction using the Strutinsky-integral method; the same Skyrme force underlay both parts of the calculation. Here, in our HFB calculations, the ETF method is retained for determining the initial mean field. Now deformations in the ETF method are described by the (c, α, h) parameters of Brack et al. [43], and so the same parametrization will have to be adopted in the HFB calculations. We recall that these parameters describe the shape of a reference surface $S_0(c, \alpha, h)$ that is intended to coincide more or less with the actual surface of the fissioning nucleus, or with the two fragments after fission; c relates to the elongation, h to the necking, and α to the left-right asymmetry. With this parametrization it is possible to start with a spherical configuration and generate a continuous sequence of axially symmetric deformed shapes of a given nucleus, right up to and beyond the breakup into two separated fragments. Now in performing constrained HFB calculations in which the deformation of the initial field has been fixed by selecting a particular set of (c, α, h) parameters, as described in the following, it will be necessary to relate these latter parameters to the constraining multipole moments Q_{2c}, Q_{3c}, and Q_{4c}. This is done at the end of the first iteration by substituting the ETF density $\tilde{\rho}$, generated as described in Ref. [18], into Eq. (13). The constrained HFB iterations then proceed without further reference to the ETF method. Whenever we specify saddle-point deformations in this paper we do so not in terms of the multipole moments Q_2, Q_3, and Q_4 but rather in terms of the corresponding β_2, β_3 and β_4 parameters, defined by

$$\beta_l = \frac{\sqrt{(2l+1)\pi}}{3AR_0^l} Q_l, \qquad (17)$$

where by convention [44] $R_0 = 1.2A^{1/3}$ fm. (We stress that Eq. (17) is not exact and that in all our mass tables the ground-state deformation parameters are given through the more exact Eq. (8) of Ref. [39].)

Because of the finite dimensionality of the oscillator basis it is essential that the oscillator strengths involved in-the HFB calculations, $\omega_\perp$ for the (x, y) plane and ω_z for the symmetry axis (z direction), be optimized with respect to the deformation parameters (c, α, h), as well as to z and N. Since precisely the same problem had to be resolved in the shell-correction part of the original ETFSI barrier calculations [15] we shall make the same choice here,

$$\omega_z = \frac{k}{cA^{1/3}} \qquad (18a)$$

and

$$\omega_\perp = \omega_z / t_{\max}, \qquad (18b)$$

where $t_{\max}$ is related to the maximum width of the reference surface in the (x, y) plane [15], and k is given by Eq. (19) of Ref. [15].

The determination of barrier heights is numerically an easy task in the case of just two deformation parameters: With the total energy E_{tot} of the given nucleus calculated at a sufficient number of deformations one just makes a contour plot of E_{tot} in the (c, h) plane. However, this procedure is not available in the present case, as we admit a left-right asymmetry, and thus have to determine the fission path in the three-dimensional

space spanned by the variables (c, α, h). A solution to this problem is provided by the flooding model of Tondeur [45]. In two dimensions we imagine water being poured into a model of the energy surface, and we observe its depth, measured from the lowest point (i.e., at the ground state) as it spills over the various barriers. The virtue of this method, as compared to that of the two-dimensional contour plot, is that it can be generalized to an arbitrary number of dimensions; see Ref. [15] for a detailed account. (It turns out furthermore that the method has a venerable pedigree, going back to Maxwell [46] and even earlier [47].)

Without the flooding model we would have had to confine the determination of the fission path to the (c, h) plane, and at each point in this plane we would have had to minimize with respect to α (if this degree of freedom had been admitted into the calculation of the energy). As emphasized by Möller *et al.* [14] (and references quoted therein), such a procedure can lead to discontinuities in the fission path in a higher dimensional space, as it flips from one hypervalley to another, regardless of any hyper-ridges that might lie between the hyper-valleys. (To see this, imagine that we have been working in two dimensions, c and h, and then reduce to one dimension by minimizing with respect to h at each value of c.) This problem will arise whatever method is used to calculate the energy, as is made clear in Ref. [14] in criticizing all previous calculations of barriers made without the flooding algorithm. But although this criticism certainly applies to all previous constrained HF calculations, it must not be concluded that the problem is inherent in the constrained HF method itself: It can be avoided by use of the flooding algorithm, as in the present work. We stress that we adopt here exactly the same strategy to track the evolution of the fission path in the (c, α, h) hyperplane as did the earlier ETFSI calculations [15,16]; note particularly that although the primary variables are still c, α, and h, the constrained parameters Q_{2c}, Q_{3c}, and Q_{4c} are continuous functions of these variables.

Of course, it can be argued that even three constrained variables are not enough: With the HFB calculation automatically minimizing the energy with respect to all the other numerous degrees of freedom the fission path could be showing discontinuities in spaces of four or more dimensions. However, this problem will be serious only to the extent that the fission path flips across high hyper-ridges, which will not be the case if the three constrained variables embody the essential physics of the fissioning nucleus. Now the liquid-drop calculation of Ref. [14] tracks the fission path in five dimensions, the extra dimensions corresponding to the configurations of the separated fragments. These parameters will presumably be important after scission, but if one is interested primarily in finding barrier heights, as here, they should play a relatively minor role. Nevertheless, it might be of interest at some future date to extend the present calculations to include a constraint on the Q_5 and Q_6 multipole moments: $n + 1$ dimensions will always be better than n. But a better investment of computational effort would be to break axial symmetry and include the triaxial degree of freedom, which is neglected both here and in Ref. [14] (see, however, Ref. [30], which includes both triaxiality and left-right asymmetry, but not simultaneously).

In all cases we begin with a first HF calculation of the energy surface, assuming left-right symmetry ($\alpha = 0$). If the corresponding ETFSI calculation [15] indicates that a particular barrier in this surface is asymmetric, we calculate the HF energy surface over the (c, h) plane in the vicinity of the concerned saddle point for each of the four values of $\tilde{\alpha} = c^3 \alpha = 0.15, 0.35, 0.55, 0.75$ (note that α is never negative). The grid over the (c, h) plane corresponds to $\delta c = \delta h = 0.05$. For an accurate estimate of the barrier height, every surface is interpolated in the c and h directions using the cubic spline method, and with respect to $\tilde{\alpha}$ using a Lagrange interpolation. To provide precise values of the multipole moments (or the dimensionless quadrupole moments β_l), these are interpolated as well using the same algorithm.

E. The fission barrier of ^{240}Pu as a test case

We consider the ^{240}Pu fission barrier case in some detail to illustrate our general procedure. The ^{240}Pu energy surface calculated within the HFB + PLN (BSk8) framework in the (c, h) plane for $\alpha = 0$ is shown in Fig. 5. Deformations are given in terms of mass-independent multipole moments, Eq. (17). The calculated energy of the ground state (point G in Fig. 5) is -1812.61 MeV, this compares with the measured value of -1812.67 MeV [10]. The inner barrier height (point A), measured to be of 5.8 ± 0.2 MeV [48], is predicted to be 5.9 MeV. The first shape isomeric state (point M) is at 1.914 MeV above the ground state (experimentally, about 2.25 ± 0.2 MeV
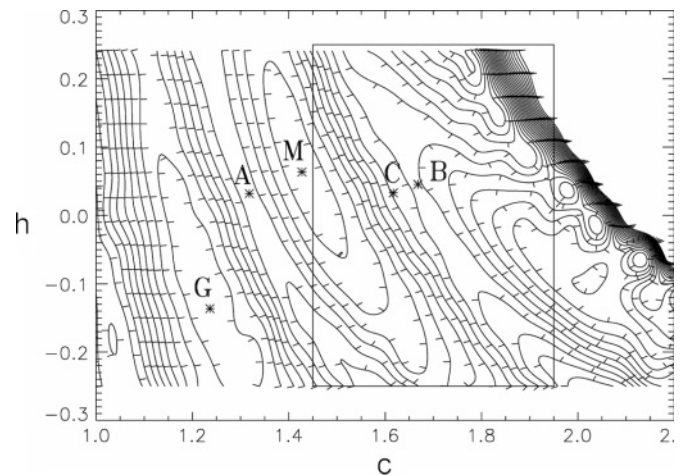
FIG. 5. Contour plot of the energy surface of ^{240}Pu in the (c, h) plane for left-right symmetry ($\alpha = 0$). The contour lines are spaced by 1 MeV. Small tick marks along each contour point in the downhill direction. G refers to the ground state ($\beta_2 = 0.276$), A to the inner saddle point ($\beta_2 = 0.545$), M to the isomeric state ($\beta_2 = 0.834$), and B to the left-right symmetric outer saddle point ($\beta_2 = 1.515$); C denotes the position in the (c, h) plane to which this saddle point shifts when left-right asymmetry is allowed ($\beta_2 = 1.267$, $\beta_3 = -0.398$). The rectangle containing B shows the limits in the (c, h) plane taken to calculate the local 3D energy surface and to locate the saddle point C. The upper right-hand zone of the panel corresponds to the fission valley, which is however reached from the lower right-hand part.
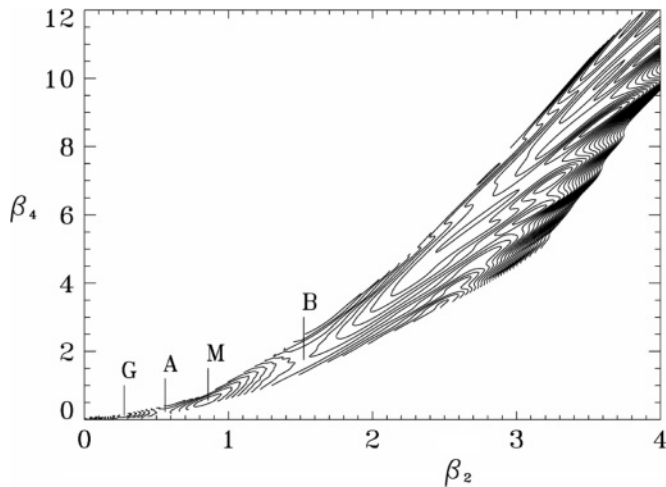
FIG. 6. Contour plot of the same energy surface as in Fig. 5, but in the $(\beta_2, \beta_4)_{\beta_3=0}$ plane.

[49]). The calculated outer barrier height for an assumed left-right symmetry is 9.6 MeV (point B). When left-right asymmetry is taken into account by including the third dimension α within a local variation of c and h over the indicated rectangle containing B, as described at the end of the previous section, the outer barrier height falls by 3.7 MeV to 5.9 MeV (point C); the measured value is 5.45 ± 0.2 MeV [49]. The role of parity projection (PP) in this case is discussed in Appendix B.

The $\alpha = 0$ energy surface plotted in the (c, h) plane in Fig. 5 is replotted in the (β_2, β_4) plane in Fig. 6; note that the relevant region of the energy surface is much narrower in this latter representation. For this reason it is much more convenient to use the (c, α, h) representation than the $(\beta_2, \beta_3, \beta_4)$ one.

III. PRELIMINARY INVESTIGATIONS

In this section we investigate the general way in which barrier heights depend on pairing strength and left-right asymmetry; the focus will be on facilitating the interpretation of the results of the next section. Note particularly that when we introduce a specific change we do not make any other compensatory changes in an attempt to refit the mass data, unlike our procedure in Sec. V.

A. Barrier height and pairing strength

It has been known for many years, at least since the work of [50], that barrier heights decrease with increasing nuclear pairing, provided left-right symmetry is imposed. It was this fact that motivated the use of a pairing strength proportional to the nuclear-surface area in the first HF calculation of a fission barrier [51], although we stress that our own calculations, based on a δ-function pairing force, do not need this feature. More recent calculations on ^{240}Pu [52] showed that an increase of pairing strength by 20% resulted in the height of the outer barrier (with left-right symmetry supposed) being reduced by approximately 30–35%.
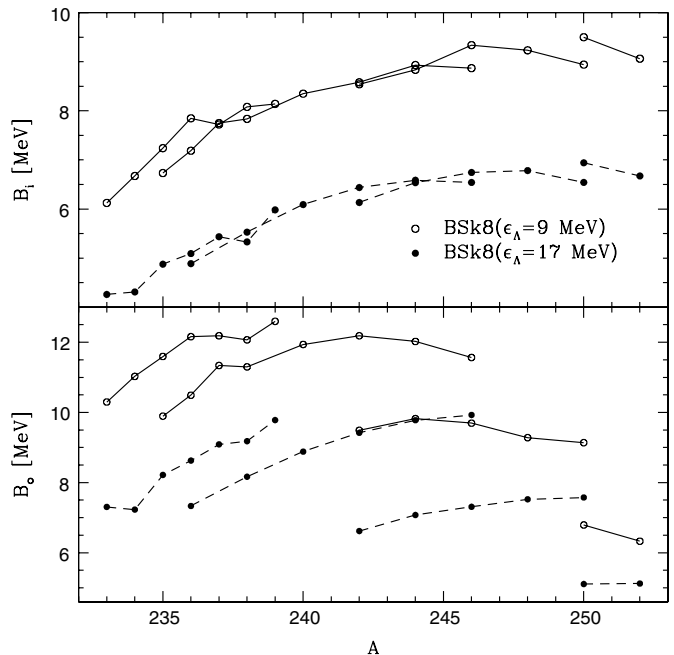
FIG. 7. Calculated inner and outer (left-right symmetric) barrier heights of some of the Np, Pu, Cm, and Cf isotopes with the HFB + PLN method; we use both the original BSk8 force and a variant in which the pairing cutoff is reduced to 9 MeV.

Figure 7 shows the results of more extensive tests that we have performed with the BSk8 force and a variant in which the pairing cutoff is reduced from $\epsilon_F \pm 17$ MeV to $\epsilon_F \pm 9$ MeV (without readjusting the Skyrme or other pairing parameters), which is equivalent to reducing the pairing strength by about 50 MeV, i.e., by 15%). We found that with the reduced pairing strength the inner barrier heights B_i of actinides increase by about 2 MeV (and in the superheavy regions, the increase can reach 4 MeV, doubling the barrier heights), whereas the outer barrier heights B_o increase by about 3 MeV (or a factor of 3 for some superheavies) if left-right symmetry is supposed.

It is easy to understand why increased pairing results in a lowering of barriers. Referring to sp level diagrams drawn as a function of deformation, it is clear that the sp level density will change with deformation. A minimum in the energy surface corresponds to a shell gap, a region of low sp level density, whereas a saddle point stands at level crossings, a region of higher sp level density, where the quasiparticles will have a broader space to occupy. The pairing therefore tends to increase the binding at saddle-point configurations more than it does at the minima, and consequently it lowers the fission barrier.

We consider now the specific case of odd nuclei. An odd-even effect, present in masses, exists also in fission barriers, with an unpaired nucleon tending to add about 0.3 MeV to the barrier height, as can be seen in the data plot in Fig. 8.

This same figure shows that the barrier heights calculated with force BSk8 likewise display an odd-even effect of about the same magnitude, but with the wrong phase, an unpaired
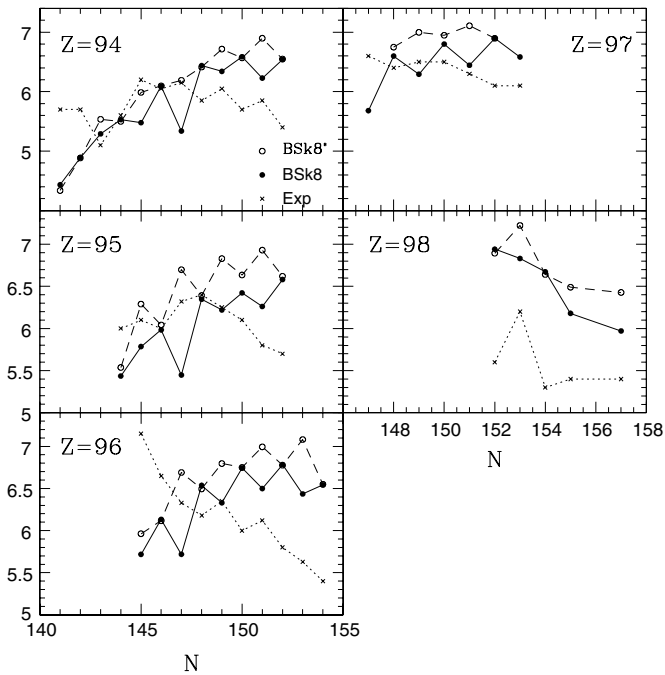
FIG. 8. Calculated inner barrier heights of the Pu, Am, Cm, Bk, and Cf isotopes compared to experimental barriers (dotted line). The HFB + PLN method is used with the Skyrme force BSk8 with staggered pairing included (solid line) and excluded (dashed line).

FIG. 9. Influence of the reflection asymmetry (including parity projection) on the symmetric outer HFB + PLN (BSk8) barrier heights for $88 \leqslant Z \leqslant 98$. The upper panel gives both reflection-symmetric and reflection-asymmetric barrier heights; the lower panel gives the difference $B_o(\alpha = 0) - B_o(\alpha > 0)$. Note that the figure does not include the comparison for the outermost third barriers observed in subactinides (see text for more details).

nucleon tending to *lower* the barrier. Given what we have said about a stronger pairing leading to lower barriers, it is easy to attribute our barrier results to the "staggering" of the BSk8 pairing (i.e., the fact that it is slightly stronger for an odd number of nucleons than for an even number). To check this we reran the calculations without staggered pairing, setting the odd-nucleon pairing strength equal to that determined for the even-nucleon pairing, and found that the odd-even effect then indeed had the correct phase, as seen in plot BSk8' of Fig. 8. However, it will also be seen that suppressing the staggered pairing exacerbates the tendency of our calculations to overestimate barrier heights in each isotope chain as N increases.

It is far from clear that suppressing the staggering of the pairing would result in any overall improvement in the fission-barrier results, and in any case the associated shifts in the barrier heights are negligible compared to all the other sources of error in our calculations, as will be seen in Sec. IV. However, it is certain that abandoning staggered pairing would lead to an unacceptable deterioration in the quality of the mass fit. Moreover, it is quite possible that the wrong phase of the odd-even effect found for BSk8 has nothing to do with pairing: Our calculations are adiabatic, in the sense that the computed fission path minimizes the total energy without taking into account the conservation of the angular momentum fixed by the unpaired nucleon. Thus on these ground alone our calculations must tend to underestimate the barrier heights of nuclei with unpaired nucleons, and it is possible that if we could take account of this effect we would find the right odd-even effect without any modification of the pairing.

B. Barrier height and reflection asymmetry

It is known from the observed experimental double-humped mass distribution of fission fragments [53] that outer fission barriers tend to be left-right reflection asymmetric for $Z \geqslant 88$. This has been confirmed in many calculations, including those that we present in Table IV. To form some idea of the extent to which this symmetry breaking is energetically favored, we have calculated the barrier heights of 91 nuclei with z ranging from 88 to 98, first with and then without left-right symmetry. The results are displayed in Fig. 9, with the lower panel giving the difference $B_o(\alpha = 0) - B_o(\alpha > 0)$.

The lowering observed in Fig. 9 resulting from the asymmetry depends on the atomic number and varies along an isotopic chain, as seen in the lower panel, which shows how the calculated effect is maximal in the vicinity of ^{232}Th and not only vanishes for $Z < 88$ but also becomes small beyond $z = 100, A = 258$.

In most of our calculations of nuclei with $Z < 92$ (Table IV) triple barriers are found, the subset of these nuclei having $Z \geqslant 88$ are also left-right asymmetric. However, for at least some nuclei in this subset, and all those appearing in Table III, the presence of the third barrier becomes clearly apparent when allowing for the breaking of left-right symmetry: If left-right symmetry is imposed all the nuclei of Table III show only two major barriers (columns A and B), but in several cases releasing the constraint reduces the second barrier (column B) enough to make the third outermost barrier dominant. This appearance of a third barrier is indicated in Table III by two entries in column C. The new shape isomer arises from the

TABLE III. Triple-humped barrier heights (in MeV) predicted by the HFB + PLN (BSk8) model for a few specific cases; experimental data are shown in parentheses.

	G	A	M	B	C
^{230}Th	−1754.68 (−1754.41)[a]	4.4 (5.4)[b]	2.58, 5.53 (2.25, 5.55)[b]	11.71	7.25, 9.21 (5.75, 6.45)[b]
^{231}Th	−1760.30 (−1759.53)[a]	4.4 (5.1)[b]	2.35, 4.81 (2.30, 5.65)[b]	11.69	7.19, 9.65 (5.90, 6.51)[b]
^{233}Th	−1771.95 (−1770.75)[a]	4.8 (5.1)[b]	2.52, 4.67 (2.30, 5.21)[b]	12.71	7.66, 10.00 (6.05, 6.82)[b]
^{237}U	−1795.37 (−1794.77)[a]	5.3 (5.1)[b]	2.19, – (2.20, 5.90)[b]	11.23	7.08, – (6.00, 5.95)[b]

[a]Reference [54].
[b]Reference [55].

fact that the effect of left-right asymmetry is small not only for very low deformations but also at very high deformations.

C. Joint influence of pairing strength and reflection asymmetry

We find that the effect of introducing left-right asymmetry is greater the weaker the pairing: In the case of ^{240}Pu breaking left-right symmetry lowers the outer barrier from 9.6 to 5.8 MeV for a cutoff of 17 MeV, but from 11.9 to 6.1 MeV for a cutoff of 9 MeV. That is, although weakening the pairing raises the barrier by 2.3 MeV for an imposed left-right symmetry, the same weakening of the pairing will raise the barrier by only 0.3 MeV when this symmetry is broken. Thus the conclusions of Sec. III A concerning the impact of pairing have to be mitigated, and it is conceivable that for a very large asymmetry weakening the pairing might even have the effect of lowering the barrier. Another consequence of this result is that the even-odd effect associated with our use of "staggered" pairing will be smoothed by the breaking of left-right symmetry. This effect is clearly visible in Fig. 9, where in some cases the staggering of the barrier height is even reversed, leading to a better agreement with experiment.

Although quite beyond the scope of the present work, it would be instructive to make a similar study for the inner barriers, determining to what extent a weaker pairing implies a stronger effect of triaxiality.

IV. COMPARISON WITH EXPERIMENTAL DATA

The comparison of reflection-*symmetric* outer barrier heights calculated with the various Skyrme forces of Table I with the experimental ones in Table IV certainly gives a criterion of selection: If, without the introduction of asymmetry, the calculated outer barrier heights do not lie above the experimental data, the corresponding Skyrme force should be rejected. BSk8 and BSk9 were the only forces we found to satisfy this criterion. In fact, BSk8 gives the best mass fit of all our forces, whereas BSk9 is our only force that correctly describes the variation of the energy per neutron of neutron matter with density. In this section the comparison with data will be made just with BSk8, calculated in the full HFB + PLN + PP model.

A. Nuclei with $80 \leqslant Z \leqslant 98$

In Table IV we compare the BSk8 results with all the data given in the IAEA compilation [48], supplemented by some other sources, as indicated in the caption to this table. B_i and B_o denote the calculated inner and outer barrier heights; we show also the corresponding calculated deformation parameters and the experimental barrier heights, where available. The double entries in the outer barrier columns correspond to the presence of a triple barrier in the computed energy surface. For the nuclei where a triple barrier has been seen experimentally, we show only the higher of the two outer ones in Table IV, with further details being given in Table III. A typical uncertainty in the experimental values, as suggested by differences among various compilations, is of the order of ± 0.5 MeV.

In discussing these results we shall pay particular attention to the primary barriers (i.e., the highest barrier for each nucleus). The primary barriers will generally be better measured than the secondary (i.e., lower lying), barriers, and they are certainly the more important of the two for the *r*-process, since they determine thresholds. Furthermore, spontaneous-fission lifetimes tend to be dominated by the primary barrier, even if occasionally a secondary barrier can have a crucial effect if it is wide enough. We show in Fig. 10 the deviations ΔB of all our calculated primary barrier heights from the measured values; in the same graph we show also the corresponding quantities for the ETFSI barrier calculations [15].

These results are most readily discussed in terms of two groups of nuclei, according to whether $Z \geqslant 92$ or $Z < 92$.

1. Uranium and beyond

In our calculations with force BSk8 we find all 58 of these nuclei to be double humped, and in all cases the agreement with the measured barrier heights is satisfactory, both for the inner and outer barriers, the discrepancy usually being under 1 MeV. The agreement is particularly good when we confine ourselves to the primary barriers (i.e., the higher of the two barriers): For these the largest discrepancy is 1.6 MeV, and we find an rms deviation of 0.722 MeV, which represents a considerable improvement when compared to the 0.972 MeV found for the ETFSI primary barriers of this group of nuclei [15]. It is gratifying to see that for this important group of nuclei the level of agreement of our model with experiment that we have obtained for the primary barriers is approaching that of the mass fits, without, it should be recalled, any further parameter adjustment. Since a significant fraction of our calculated barriers are too high, it is not clear what would happen if we were to take account of triaxiality.

TABLE IV. Experimental and BSk8 barrier heights and BSk8 deformation parameters at the inner and outer saddle points (see text for more details). Experimental barriers are from [48], except as noted.

Z	N	A	β_2	β_4	B_i	Expt.	β_2	β_3	β_4	B_o	Expt.
80	118	198	0.360	0.062	9.3	—	3.823	0.000	8.860	28.0	16.6
81	119	200	0.396	0.076	9.9	—	3.683	0.000	7.078	26.5	22.8
	120	201	0.349	0.066	11.4	—	1.597, 3.751	0.000	2.156, 8.648	20.7, 28.2	23.1
82	122	204	0.343	0.080	14.3	—	1.349, 3.748	0.000	1.496, 7.140	22.9, 29.2	23.5
	123	205	0.341	0.090	15.1	—	1.386, 3.588	0.000	1.440, 6.320	23.5, 30.1	24.6
	124	206	0.342	0.086	16.5	—	1.326, 3.170	0.000	1.492, 3.768	25.4, 30.2	25.3
	125	207	0.325	0.090	16.6	—	1.340, 3.162	0.000	1.418, 6.628	25.6, 30.2	27.0
	126	208	0.352	0.096	17.0	—	1.330, 3.449	0.000	1.296, 3.324	26.3, 31.5	27.4
83	123	206	0.335	0.092	12.6	—	1.335, 3.813	0.000	1.524, 9.730	20.3, 25.2	22.4
	124	207	0.342	0.094	14.0	—	1.310, 3.812	0.000	1.354, 6.084	22.2, 26.7	22.8
	125	208	0.325	0.094	14.0	—	1.309, 3.751	0.000	1.366, 8.454	22.5, 27.9	23.8
	126	209	0.357	0.104	15.0	—	1.308, 3.744	0.000	1.450, 7.198	23.7, 28.7	24.3
	127	210	0.350	0.106	13.6	—	1.337, 3.807	0.000	1.472, 7.046	22.7, 27.3	24.3
84	123	207	0.342	0.118	12.5	—	1.342, 3.616	0.000	1.574, 6.732	19.5, 22.5	19.3
	124	208	0.354	0.112	13.9	—	1.361, 3.681	0.000	1.468, 5.986	21.2, 24.6	19.9
	125	209	0.329	0.102	13.7	—	1.355, 3.744	0.000	1.442, 8.914	21.2, 25.1	21.1
	126	210	0.370	0.122	14.8	—	1.322, 3.562	0.000	1.366, 5.082	22.7, 25.6	21.2
	127	211	0.367	0.114	12.9	—	1.417, 3.099	0.000	1.594, 2.986	21.0, 23.5	20.6
	128	212	0.362	0.124	13.8	—	1.336, 3.568	0.000	1.480, 3.450	22.3, 25.3	19.6
85	127	212	0.374	0.114	11.3	—	1.342, 3.677	0.000	1.442, 8.452	18.7, 20.7	18.6
	128	213	0.365	0.132	12.0	—	1.347, 3.810	0.000	1.454, 8.352	19.6, 21.8	17.3
86	130	216	0.394	0.150	9.8	—	0.724, 3.509	0.000	0.654, 7.090	13.0, 18.2	13.5
88	137	225	0.447	0.130	4.3	—	1.219, 1.716	−0.462, −0.246	1.390, 2.364	7.9, 11.8	7.6
	138	226	0.452	0.138	4.4	—	1.274, 2.592	−0.562, −1.380	1.534, 4.574	8.2, 11.9	8.5
	139	227	0.509	0.164	3.8	—	1.357, 2.055	−0.548, −1.082	1.650, 3.052	8.2, 11.7	8.2
	140	228	0.471	0.160	4.5	—	1.053, 1.879	−0.122, −0.354	1.144, 2.800	8.3, 12.6	8.0
89	129	218	0.422	0.178	6.8	—	0.764, 1.244	−0.190, −0.098	0.620, 1.362	7.6, 10.7	7.4[a]
	130	219	0.430	0.168	6.4	—	0.757, 1.331	−0.182, −0.054	0.576, 1.446	7.2, 11.4	7.4[a]
	131	220	0.420	0.184	5.6	—	0.951, 1.300	0.000, −0.090	1.008, 1.484	8.9, 10.2	7.4[a]
	132	221	0.420	0.150	4.9	—	0.952, 1.487	0.000, −0.208	1.028, 1.728	8.6, 9.9	7.3[a]
	133	222	0.451	0.174	4.0	—	0.951, 1.816	0.000, −0.020	1.010, 2.646	7.4, 9.1	7.3[a]
	137	226	0.435	0.128	4.2	—	1.092, 1.765	−0.362, −0.098	1.188, 2.422	7.1, 10.4	7.8
	138	227	0.452	0.136	4.2	—	1.375, 1.590	−0.588, −0.210	1.706, 1.982	7.5, 10.7	7.4
	139	228	0.474	0.144	4.0	—	1.068, 1.666	−0.010, −0.234	1.132, 2.202	8.2, 10.4	7.1
90	130	220	0.383	0.138	5.8	—	1.115, 1.680	−0.452, −0.710	1.166, 2.340	8.9, 10.2	6.8[a]
	131	221	0.397	0.146	4.6	—	1.325	−0.158	1.354	9.0	6.7[a]
	132	222	0.417	0.140	4.2	—	1.181, 1.757	−0.410, −0.392	1.328, 2.380	7.7, 8.8	6.7[a]
	133	223	0.435	0.166	3.6	—	1.448	−0.274	1.654	8.0	6.9[a]
	137	227	0.443	0.124	3.9	5.9	1.310, 2.094	−0.606, −0.626	1.604, 3.340	6.8, 9.2	6.6
	138	228	0.465	0.132	4.0	6.2	1.287, 2.426	−0.578, −1.248	1.582, 4.036	7.0, 8.9	6.5
	139	229	0.508	0.164	3.7	5.9	1.560, 2.539	−0.692, −1.328	1.946, 4.440	7.1, 9.5	6.3
	140	230	0.491	0.152	4.4	5.4[b]	1.231, 2.561	−0.438, −1.380	1.408, 4.542	7.2, 9.2	6.5[b]
	141	231	0.522	0.154	4.4	5.1[b]	1.324, 2.498	−0.486, −1.148	1.618, 4.200	7.2, 9.6	6.5[b]
	142	232	0.507	0.166	4.8	5.8	1.529, 2.468	−0.620, −1.126	1.870, 4.128	7.7, 9.8	6.7
	143	233	0.538	0.222	4.8	5.1[b]	1.295, 2.626	−0.398, −1.248	1.472, 4.586	7.7, 10.0	6.8[b]
	144	234	0.533	0.194	5.4	6.1	1.315, 2.597	−0.414, −1.188	1.502, 4.496	8.0, 10.1	6.3
91	139	230	0.490	0.152	3.5	5.6	1.145, 2.431	−0.266, −1.192	1.250, 4.010	6.3, 7.3	5.8
	140	231	0.497	0.152	4.1	5.5	1.647, 2.593	−0.678, −1.260	2.264, 4.836	6.8, 8.1	5.5
	141	232	0.527	0.166	4.1	5.0	1.224, 2.590	−0.408, −1.258	1.398, 4.844	6.7, 8.1	6.4
	142	233	0.500	0.166	4.6	5.7	1.184, 2.646	−0.442, −1.234	1.362, 4.858	7.2, 8.3	5.8
92	139	231	0.498	0.148	3.7	4.4	1.133	−0.014	1.268	6.3	5.5
	140	232	0.505	0.148	4.2	4.9	1.308	−0.440	1.522	6.1	5.4
	141	233	0.526	0.188	4.3	4.4	1.249	−0.482	1.506	6.5	5.6
	142	234	0.520	0.166	4.8	4.8	1.340	−0.416	1.548	6.6	5.5
	143	235	0.513	0.170	5.1	5.3	1.251	−0.408	1.210	6.6	6.0
	144	236	0.540	0.190	5.4	5.0	1.259	−0.412	1.384	6.8	5.7

TABLE IV. (*Continued.*)

Z	N	A	β_2	β_4	B_i	Expt.	β_2	β_3	β_4	B_o	Expt.
	145	237	0.554	0.220	5.3	5.1[b]	1.442	−0.470	1.690	7.1	6.0[b]
	146	238	0.535	0.212	5.9	6.3	1.222	−0.398	1.400	7.2	5.5
	147	239	0.544	0.168	5.4	6.5	1.348	−0.454	1.572	7.0	6.0
	148	240	0.539	0.238	6.2	6.1	1.346	−0.456	1.580	7.5	5.8
93	140	233	0.504	0.186	4.1	5.0	1.249	−0.416	1.344	5.1	5.1
	141	234	0.539	0.216	4.1	5.5	1.426	−0.520	1.694	5.1	5.4
	142	235	0.547	0.218	4.7	5.5	1.527	−0.542	1.782	5.7	5.5
	143	236	0.548	0.232	4.9	5.9	1.410	−0.508	1.702	5.7	5.4
	144	237	0.548	0.230	5.3	6.0	1.486	−0.520	1.762	5.9	5.4
	145	238	0.574	0.248	5.1	6.5	1.266	−0.372	1.340	6.2	5.8
94	141	235	0.515	0.152	4.3	<5.7	1.187	−0.388	1.218	4.7	5.1
	142	236	0.530	0.178	4.7	<5.7	1.385	−0.446	1.590	5.0	4.5
	143	237	0.537	0.182	5.1	5.1	1.285	−0.402	1.514	5.3	5.2
	144	238	0.543	0.206	5.4	5.6	1.235	−0.408	0.770	5.4	5.1
	145	239	0.560	0.228	5.3	6.2	1.269	−0.362	1.272	5.8	5.7
	146	240	0.561	0.226	5.9	6.1	1.267	−0.398	1.372	5.9	5.2
	147	241	0.553	0.224	5.2	6.2	1.304	−0.378	1.426	5.4	5.5
	148	242	0.545	0.224	6.3	5.9	1.312	−0.420	1.514	6.3	5.1
	149	243	0.570	0.244	6.2	6.1	1.325	−0.386	1.452	6.3	5.5
	150	244	0.554	0.242	6.5	5.7	1.310	−0.396	1.446	6.9	4.9
	151	245	0.582	0.284	6.2	5.9	1.349	−0.428	1.492	6.6	5.3
	152	246	0.555	0.268	6.5	5.4	1.331	−0.380	1.484	6.9	5.3
95	144	239	0.543	0.208	5.3	6.0	1.292	−0.424	1.428	4.6	5.4
	145	240	0.565	0.254	5.5	6.1	1.271	−0.388	1.418	4.9	6.0
	146	241	0.538	0.224	5.8	6.0	1.203	−0.358	1.332	5.0	5.4
	147	242	0.559	0.230	5.3	6.3	1.300	−0.384	1.428	4.5	5.8
	148	243	0.544	0.230	6.2	6.4	1.302	−0.354	1.396	5.5	5.1
	149	244	0.564	0.238	6.0	6.3	1.309	−0.356	1.430	5.4	5.9
	150	245	0.555	0.256	6.3	6.1	1.330	−0.402	1.492	5.8	5.2
	151	246	0.580	0.280	6.2	5.8	1.336	−0.398	1.518	5.6	5.0
	152	247	0.554	0.260	6.5	5.7	1.358	−0.392	1.518	6.2	4.8
96	145	241	0.566	0.262	5.6	7.2	1.290	−0.362	1.412	4.5	5.5
	146	242	0.539	0.196	6.0	6.7	1.267	−0.328	1.306	4.8	5.0
	147	243	0.576	0.226	5.6	6.3	1.317	−0.372	1.464	4.4	5.4
	148	244	0.553	0.226	6.4	6.2	1.282	−0.326	1.420	5.0	5.1
	149	245	0.559	0.236	6.2	6.4	1.308	−0.368	1.436	4.9	5.5
	150	246	0.555	0.242	6.7	6.0	1.284	−0.322	1.374	5.3	4.8
	151	247	0.573	0.284	6.4	6.1	1.296	−0.364	1.468	5.1	5.1
	152	248	0.572	0.286	6.7	5.8	1.315	−0.362	1.468	5.7	4.8
	153	249	0.601	0.358	6.4	5.6	1.302	−0.396	1.552	5.5	5.0
	154	250	0.589	0.292	6.5	5.4	1.286	−0.324	1.356	5.9	4.4
97	147	244	0.567	0.228	5.5	6.6[c]	1.277	−0.322	1.390	3.8	4.2[c]
	148	245	0.542	0.212	6.4	6.4[c]	1.280	−0.352	1.382	4.3	4.2[c]
	149	246	0.552	0.230	6.1	6.5[c]	1.292	−0.364	1.442	4.2	4.7[c]
	150	247	0.551	0.230	6.7	6.5[c]	1.280	−0.328	1.324	4.8	4.6[c]
	151	248	0.568	0.326	6.4	6.3[c]	1.286	−0.320	1.382	4.6	4.8[c]
	152	249	0.580	0.262	6.8	6.1[c]	1.307	−0.334	1.378	5.1	4.5[c]
	153	250	0.565	0.240	6.5	6.1[c]	1.253	−0.364	1.454	4.8	4.1[c]
98	152	250	0.581	0.276	6.8	5.6[c]	1.310	−0.332	1.434	4.3	3.8[c]
	153	251	0.569	0.228	6.7	6.2[c]	1.312	−0.372	1.554	4.3	3.9[c]
	154	252	0.572	0.298	6.7	5.3[c]	1.342	−0.334	1.496	4.4	3.5[c]
	155	253	0.589	0.308	6.1	5.4[c]	1.333	−0.310	1.454	4.3	3.5[c]
	157	255	0.579	0.290	5.9	5.4[d]	1.351	−0.294	1.468	4.3	—

[a]References [15,56].

[b]Reference [55].

[c]Reference [57].

[d]Reference [58].
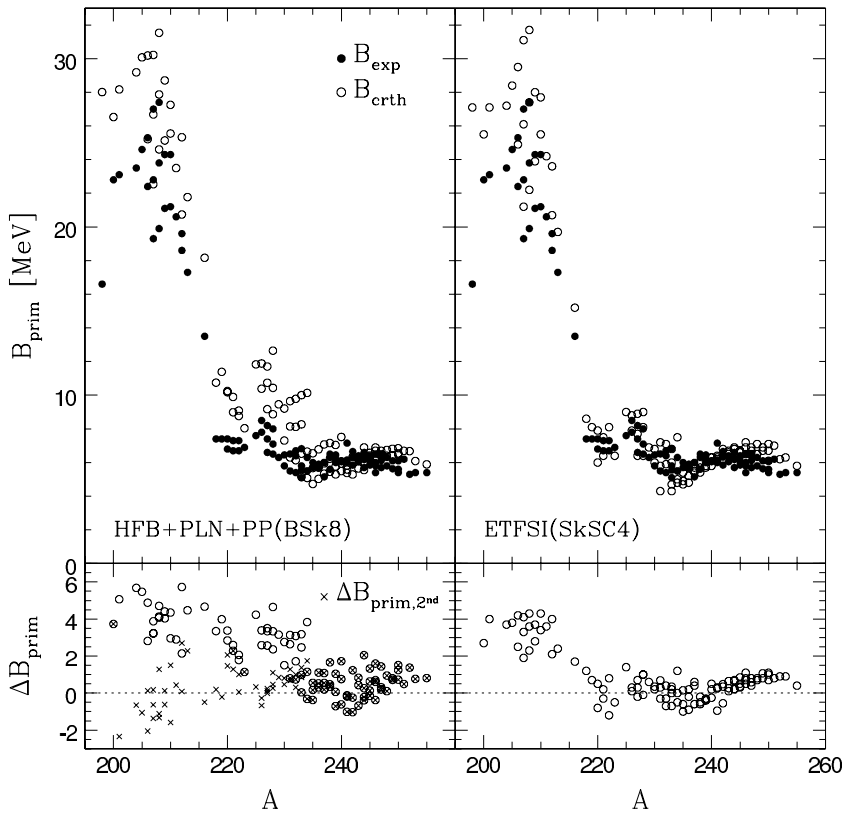
FIG. 10. Comparison with experiment of primary barriers calculated within the HFB + PLN + PP (BSk8) and ETFSI (SkSC4) frameworks. In each case we show the deviation ΔB (theory − experiment). The crosses in the lower left panel indicate the deviation ΔB between the second barrier and the experimental data whenever a triple-humped barrier is predicted.

2. Suburanics

The situation is more complex and less satisfactory for this group of nuclei. In all but four cases we find the energy surface to have a triple-humped barrier. The innermost barriers are always the lowest, and our calculated values tend to be 1 or 2 MeV lower than the measured values, for the few cases where these are available. Our outermost barriers are always the highest (i.e., the primary barriers), and they are invariably too high, the deviation from the measured value typically ranging from 2 to 5 MeV, but occasionally higher. These results are significantly worse than those for the ETFSI calculations of this group of nuclei [15]. They also conflict with the much better results obtained using force MSk7 in Hartree-Fock-BCS (HFBCS) calculations [59]. This suggests that the problem may well lie with the choice of force; we return to this point in the following.

3. General discussion

The sudden deterioration as we pass from $z = 92$ to $z = 91$ in the agreement between our results and the measured values of the primary-barrier heights is seen to be correlated with a jump in the values of all three of the corresponding deformation parameters. A similar behavior is found with the ETFSI calculations, but there the discontinuity occurs on passing from $z = 88$ to $z = 86$ (as there are no data for $z = 87$). Thus, although ETFSI can predict all measured primary barriers for $Z \geqslant 88$ to within 1.4 MeV, a similar level of precision with the present calculations is achieved only for $Z \geqslant 92$.

The onset of a sudden deterioration in our results as we pass from $z = 92$ to $z = 91$ also coincides with the appearance of triple barriers in our calculated energy surfaces: All but four of our nuclei with $Z < 92$ show this feature. Thus the question arises as to whether the triple barriers that we find are real or not. Experimentally, it has been shown that triple-humped barriers could well exist [55] in ^{230,231,233}Th and ^{237}U, as we have indicated in Table III, but there is certainly no experimental confirmation for all the triple barriers that we predict.

Interestingly, whenever we have a triple barrier it is found that the intermediate saddle point is located at a deformation of about $\beta_2 \approx 1.3$, similar to the β_2 of the outer saddle point of the heavier actinides (which have only a double barrier), and the corresponding height is in much better agreement with the experimental data (as indicated by the crosses in the lower left panel of Fig. 9.) Clearly, at least a part of our problem must be connected with the appearance of a third barrier; more generally, our calculated energy is too high at large deformations.

To investigate this matter further we have recalculated all the nuclei with $80 \leqslant Z \leqslant 86$ using the force SLy6$^{\delta\rho}$ in the HFBCS + PLN approximation. (All these nuclei are left-right symmetric.) The results of these calculations are given in Table V, which shows for each nucleus the height of the outer barrier and, in the case of a triple barrier, the intermediate barrier, together with the corresponding deformation parameters β_2 and β_4. Remarkably, in all but one case where BSk8 leads to a triple barrier, SLy6$^{\delta\rho}$ predicts a double barrier, and in the only two cases where BSk8 leads to a double barrier, SLy6$^{\delta\rho}$ predicts a triple barrier. (Note in

TABLE V. HFBCS + PLN(SLy6$^{\delta\rho}$) outer barrier heights for $80 \leqslant Z \leqslant 86$. Triple-humped barriers are predicted for $Z = 80, 81$ only.

Z	N	A	β_2	β_4	B_o
80	118	198	1.567, 3.796	1.924, 9.624	17.2, 19.8
81	119	200	1.355, 3.788	1.410, 8.504	18.5, 19.3
	120	201	1.549, 3.761	1.838, 9.760	20.1, 21.5
82	122	204	1.355	1.404	23.2
	123	205	1.249	1.258	27.2
	124	206	1.284	1.266	26.6
	125	207	1.286	1.392	30.4
	126	208	1.334	1.400	30.8
83	123	206	1.307	1.334	23.4
	124	207	1.310	1.286	24.6
	125	208	1.328	1.296	28.5
	126	209	1.361	1.420	28.7
	127	210	1.331	1.364	29.2
84	123	207	1.278	1.272	21.4
	124	208	1.294	1.266	22.6
	125	209	1.309	1.248	27.0
	126	210	1.323	1.350	26.3
	127	211	1.293	1.294	27.1
	128	212	1.323	1.390	23.2
85	127	212	1.295	1.282	24.1
	128	213	1.342	1.402	21.3
86	130	216	1.322	1.390	16.9

particular that SLy6$^{\delta\rho}$ predicts ^{230}Th to have a double barrier, in contradiction with experiment.) This shows how sensitive the position of the saddle points is to the choice of force and that the excessively high barriers obtained for BSk8 cannot be attributed to computational error. The choice of force must surely be an important factor, but this does not mean that the problem must lie with BSk8, since it is also possible that at large deformations it is not sufficient to take Q_2, Q_3, and Q_4 as constrained degrees of freedom; that is, a deformation space of higher dimensionality might be required. In any case, if a modification of the force is needed, a force resembling more closely SLy6$^{\delta\rho}$ cannot be the solution, since its barriers are seen from Table V to be even higher than those of BSk8 in some cases.

It would always be possible for us to significantly lower our outermost barriers by invoking a deformation-dependent Wigner term with an $|N - Z|$ factor. However, we do not resort to this device, since, as we argued in Sec. II, the only independent evidence that is relevant points against the existence of such a term.

A final remark on the experimental barrier heights that we have used is in order. These are not directly measured quantities, depending rather on a model-dependent analysis of the raw experimental data. Since the model usually adopted is that of the double barrier, some error will be introduced in the case of triple barriers, and it would be better if a more sophisticated model for the data analysis could be used. Moreover, it should not be forgotten that our barrier calculations are static and that dynamic corrections, of the type considered in Ref. [60], might play a role. However, it is far from clear that these different factors lie at the heart of the problems that we have reported here.

B. Barriers of superheavy elements

Of the superheavy (SH) nuclei shown in Table VI, data are available only for three, ^{286}112, ^{292}114, and ^{296}116. Moreover, although only lower limits on the barrier heights are given, it should be emphasized that even these are highly tenuous. The corresponding nuclei are produced by the fusion-fission reactions ^{48}Ca + ^{238}U, ^{48}Ca + ^{244}Pu, and ^{48}Ca + ^{248}Cm and the quoted values [61] come from an optimal fit of the

TABLE VI. Ground states and fission barriers of some SH nuclei calculated with forces BSk8 and BSk9 in the HFB + PLN framework with reflection asymmetry allowed. (Only one barrier is found in SH nuclei.) The columns labeled BSk8^9 and BSk8^5 refer to pairing-modifed versions of BSk8, as described in the text; these two calculations were performed with reflection symmetry imposed. Also shown are the barrier data and the results for the ETFSI (SkSC4) model [16]. Dashes mean not measured or not calculated.

Z	N	A	M(BSk8) (β_2)	B_i(Exp)	BSk8 (β_2)	BSk9	BSk8^9	BSk8^5	SkSC4
112	172	284	163.443 (0.1246)	—	0.94 (0.300)	1.08	5.31	6.58	2.18
	174	286	167.039 (0.1045)	$\geqslant 5.5$	1.28 (0.290)	1.54	5.72	7.18	3.55
	176	288	171.098 (0.0762)	—	1.72 (0.271)	1.98	6.04	7.58	4.79
	178	290	175.598 (0.0658)	—	1.97 (0.253)	2.29	6.28	7.63	5.83
114	178	292	183.609 (0.0458)	$\geqslant 6.7$	2.43 (0.262)	2.79	7.03	9.97	7.24
116	180	296	196.739 (0.0226)	$\geqslant 6.4$	3.10 (0.248)	3.44	8.84	12.65	7.60
	184	300	194.959 (0.0615)	—	3.34 (0.247)	3.48	8.50	11.95	7.70
118	184	302	204.151 (0.0607)	—	3.96 (0.234)	3.92	9.00	12.53	7.40
120	172	292	203.808 (0.0676)	—	3.86 (0.249)	—	—	—	4.90
	184	304	215.224 (0.0461)	—	4.36 (0.234)	4.24	8.95	12.39	6.80
122	184	306	228.164 (0.0429)	—	4.27 (0.223)	4.29	8.44	11.84	—
124	184	308	243.094 (0.0356)	—	3.59 (0.212)	4.04	7.59	10.66	—
126	184	310	259.394 (0.0264)	—	2.81 (0.190)	3.49	6.13	8.93	—
128	184	312	277.406 (0.0235)	—	1.95 (0.181)	2.92	4.64	6.89	—
130	184	314	296.770 (0.0363)	—	1.07 (0.156)	2.21	3.49	5.24	—

parameters entering the theoretical analytical expression of the measured cross section of the yield of a heavy evaporation residue nucleus. (Owing to an uncertainty in the assignment of the neutron number, the same experimental barrier applies also for their lighter isotopes.) Some of the numerous parameters that are required for the analysis are determined by assuming the validity of the LDM and the FRDM for $Z = 102$ isotopes (produced in the ^{48}Ca + $^{204-208}$Pb reaction), whose decay properties are predicted to be very close to those of SH nuclei [61]. The use of such a very indirect method clearly shows the difficulty of obtaining information on barriers of SH nuclei, even though it is clear that these nuclei fission. These barrier data can therefore serve as no more than a preliminary guide. Nevertheless, the ETFSI (SkSC4) results [16], given in the last column, are in very good agreement with these data, predicting as well the asymmetric character of ^{296}116 (cf. Fig. 5 (c) of [61]).

We show in Table VI the results of barrier calculations for both forces BSk8 and BSk9, made within the HFB + PLN framework, and with reflection asymmetry being allowed; only one barrier is found in SH nuclei. Both these forces are seen to give barriers that are far too low, with the BSk9 barriers being almost always slightly higher. Since the higher symmetry coefficient of BSk9 ($J = 30$ MeV, as opposed to 28 MeV for BSk8) should have the effect of slightly lowering the barrier (see Sec. V C), the higher barriers found in SH nuclei for force BSk9 must be due to the weaker pairing of this force, in accordance with Sec. III A.

Indeed, since SH nuclei are stabilized exclusively by microscopic effects [62] we can expect their barriers to be exceptionally sensitive to the pairing strength. We investigate this point further by repeating the calculations, with two pairing-weakened versions of BSk8, labeled BSk8^9 and BSk8^5, these being characterized by pairing cutoffs at 9 and 5 MeV, respectively, as opposed to the 17 MeV of the original BSk8 force. These new calculations are performed with reflection symmetry imposed. With the cutoff at 9 MeV, corresponding to a reduction of 15% of the BSk8 pairing strength, the barrier heights are comparable to the experimental values, although the calculated pairing gaps are slightly too large; inclusion of reflection asymmetry would probably have lowered the barriers. With the cutoff at 5 MeV, corresponding to a reduction of 60% of the BSk8 pairing strength, the experimental gaps are well fitted, as in other Skyrme-Hartree-Fock calculations [12,63], but the SH barriers become rather high. However, the inclusion of triaxiality and reflection asymmetry are crucial in this respect. Generally speaking, with the cutoff at 5 MeV our results begin to be in quantitative agreement with the mean field of Refs. [12,63]. Although it will be a challenging task to reduce the pairing strength by 15% if masses are still to be fitted, a further decrease will certainly need modifications or improvements at and beyond the mean-field approximation.

V. COMPARISON OF BARRIERS GIVEN BY DIFFERENT MASS MODELS

Only one force, BSk8, was used for the complete calculations of the experimentally known fission barriers, since,

as already explained, preliminary calculations showed that all the previously constructed forces would give barriers that were systematically too low. Fortunately, BSk8 also gives the best mass fit of all our forces. (We will see in the following that BSk9 gives barriers that are very similar to those of BSk8, for nuclei not too far from stability.) Nevertheless, it is of some interest to compare with the barrier predictions for other forces, with a view both to understanding why BSk8 (along with BSk9) works better than the other forces, and to point the way to further improvements.

The evolution of our family of forces was such that it is possible to compare pairs of forces that differ with respect to just one imposed physical characteristic or model feature, while maintaining an optimal fit to the mass data. For example, BSk2 and BSk6 differ only with respect to the value of the imposed isoscalar effective mass M_s^*, BSk6 and BSk7 with respect to the density dependence of the pairing, and BSk8 and BSk9 with respect to the imposed volume symmetry coefficient. For BSk6 and BSk8, the situation is slightly different, since these are identical in their imposed physical characteristics but differ in that the latter has number projection (PLN) built into its model. Likewise BSk1 and BSk2 differ in the way their respective models treat the pairing cutoff. Of course, restoring the mass fit will result in other changes arising, effectively to compensate the imposed change.

Given the computational expense of the full HFB + PLN method we decided, before making these supplementary calculations, to see to what extent it is legitimate, within the context of fission barriers, to make simplifying approximations to the full method. We deal with this question in the following subsection.

A. Sensitivity of barriers to the global framework: From HFBCS to HFB + PLN

Figure 11 displays the fission barrier heights of the Pu isotopic chain for four different microscopic methods, all based on the same BSk8 Skyrme force: the HFBCS, HFBCS + PLN, HFB, and HFB + PLN approximations.
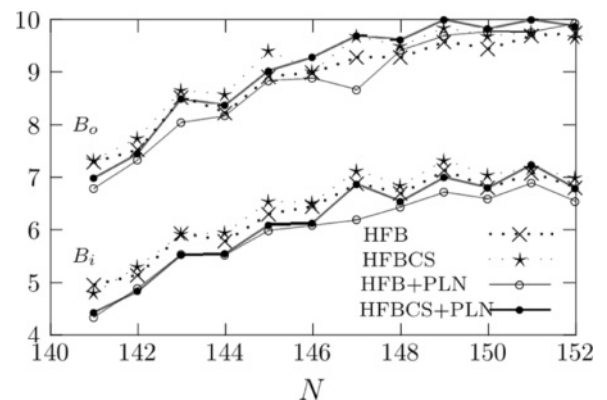
FIG. 11. Inner (B_i) and outer (B_o) barrier heights of Pu isotopes calculated with Skyrme force BSk8 with four methods: HFBCS (stars), HFBCS + PLN (full dots), HFB (crosses), and HFB + PLN (circles); reflection symmetry is imposed.

It is seen that all methods are more or less equivalent within ±0.5 MeV, at least in the prediction of the axially and reflection-symmetric fission barriers of Pu isotopes that are not very far from the stability line, but it should be noted that we have not tested nuclei with a large neutron excess. And in any case, the equivalence will certainly not hold for absolute ground-state energies; it holds here only because a barrier height is a difference of two energies, and thus less sensitive than masses, for example, to the method. In the comparative study made in the rest of this section, barriers will be calculated in the HFBCS approximation for forces BSk1, BSk2, BSk6, and BSk7, whereas the HFB + PLN method is retained for the BSk8 and BSk9 forces.

B. Comparison of BSk6 and BSk8: Role of surface coefficient a_{sf}^0

The barrier heights of 114 nuclei for which one or both barrier heights are known are compared for forces BSk6 and BSk8 in Fig. 12, where it will be seen that the barriers for the latter are substantially higher than those of the former; the difference is of the order of 1 MeV for the inner barriers and between 2 to 4 MeV for the outer barriers (except for Ra and Ac). In fact, as we have already pointed out, BSk8 is the first of our forces to give barriers that were not systematically too low. But BSk6 and BSk8 are very similar forces in that they have been constrained to the same physical characteristics, for example, the same values of the symmetry coefficient ($J = 28$ MeV) and of the isoscalar effective mass ($M_s^* = 0.8$). The only major difference comes from the framework in which they have been fitted, HFB for BSk6 and HFB + PLN for BSk8, and it is of obvious interest to see how the PLN particle-number projection should have led to such a crucial improvement.

The incorporation of the PLN method in the HFB model cannot itself explain such a drastic change, since we have shown here (Sec. V A) that *for a given force* the PLN projection has no significant effect on barrier heights (in fact, insofar as there is any change at all, we see from Fig. 11 that the use of the full HFB + PLN method should lead to a slight lowering of the barriers). But the two forces BSk6 and BSk8 are not, of course, identical, because the HFB and HFB + PLN methods are not equivalent at the level of the mass fits. Inspection of Table II shows that the only macroscopic parameter that differs substantially between the two forces is the surface coefficient a_{sf}^0, which is 0.46 MeV higher for BSk8. The effective surface coefficient $a_{sf}(I)$ for ^{240}Pu, as given by Eq. (6), is similarly higher for BSk8, which is sufficient to account for the higher barrier: A gross estimate made by assuming a spherical nucleus fissioning into two spherical fragments leads to the barrier height increasing by around $10 \, \delta a_{sf}(^{240}\text{Pu}) = 4.6$ MeV.

This sensitivity of barrier heights to a_{sf}^0 was well established some years ago in Ref. [64], where an increase of 0.65 MeV in a_{sf}^0 led to the ^{240}Pu barrier height of the original SkM force being raised from 1.5 to 3.5 MeV (with the new force subsequently named SkM*). It also appears from [64] that the effect of the surface tension on the energy surface increases with deformation, simply because the area increases.

To recapitulate, the increase in surface energy that we have obtained in going from BSk6 to BSk8 is a consequence of the PLN particle-number projection with the latter force, but the precise mechanism in play here is not at all clear to us. Moreover, we hesitate to affirm that PLN must be an essential feature of any successful microscopic calculation of fission barriers: The fact that the barriers of forces BSk1-7 are too low could simply be a result of too strong a pairing.
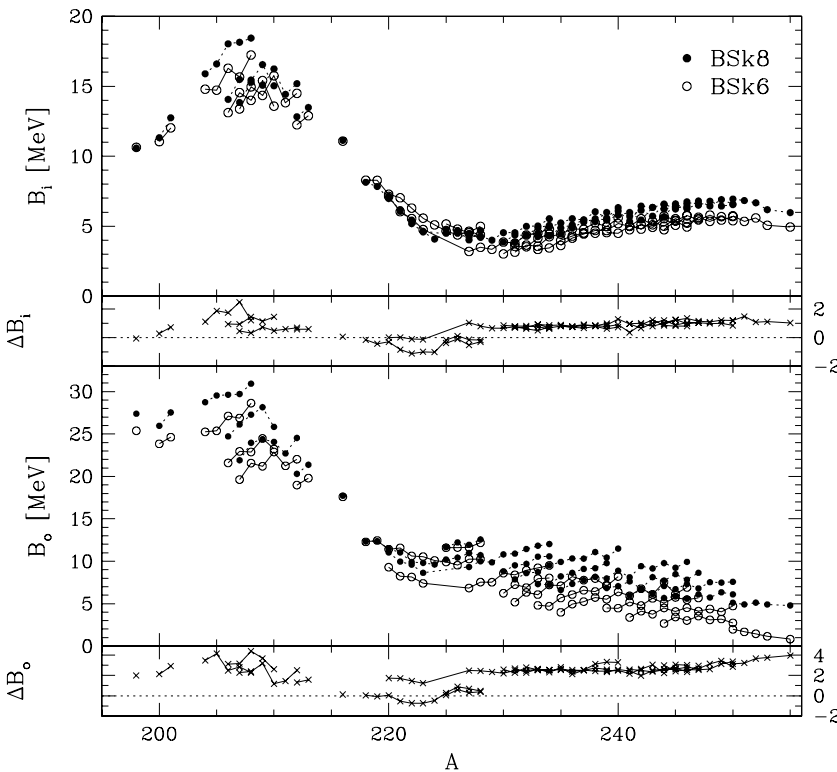
FIG. 12. HFB + PLN (BSk8) inner and outer barrier heights compared to those of HFBCS (BSk6); $\Delta B_{i,o} = B_{i,o}(\text{BSk8}) - B_{i,o}(\text{BSk6})$ (in MeV).

C. Comparison of BSk8 and BSk9: Role of symmetry coefficient J

The only imposed difference between BSk8 and BSk9 lies in their respective values of the volume symmetry coefficient J: 28 MeV for the former and 30 MeV for the latter. This increase in J results in a slight deterioration of the quality of the mass fit [8], but there are compelling reasons for believing that J must be *at least* 30 MeV, even if free Skyrme-force fits to masses always seem to lead to a value lying around 27.5 MeV [8]. As always, the mass fit imposes an anticorrelation between J and the surface-symmetry coefficient a_{ss}, defined in Eq. (5) [8]. However, the reduction in a_{ss} associated with the increase in J is itself offset by a small increase in a_{sf}^0, but the effective surface coefficient $a_{sf}(I)$ defined in Eq. (6) will nevertheless be smaller for BSk9 than for BSk8 if $I > 0.14$, which is the case for all the nuclei considered here. Thus we should expect BSk9 to give lower barriers than does BSk8 for all nuclei, with the effect becoming accentuated as we move toward the neutron drip line. (This anticorrelation between barrier height and J is discussed in more detail in Ref. [16].)

We show in Fig. 13 the barrier heights that we find with both forces for even-even isotopes of Ra, Th, U, Pu, Cm, and Cf close to the stability line. It will be seen that as N increases the BSk9 outer barriers do become progressively lower than those of BSk8, as expected. As discussed in Sec. VI, this trend becomes very pronounced as the neutron drip line is approached (see especially Table VII).

D. Comparison of BSk2 and BSk6: Role of the isoscalar effective mass M_s^*

Figure 14 compares the inner and outer barrier heights for some 114 nuclei obtained with the Skyrme forces BSk2 and BSk6, which differ in that different values of the isoscalar effective mass have been imposed. No significant difference between the two forces is apparent, and we conclude that barriers are not very sensitive to the choice of effective mass, at least for the nuclei considered here, once the Skyrme and pairing-force constants have been adjusted to maintain the mass fit.

It will be seen from Table I that the pairing is much stronger for BSk6 than for BSk2. The effect of the increased
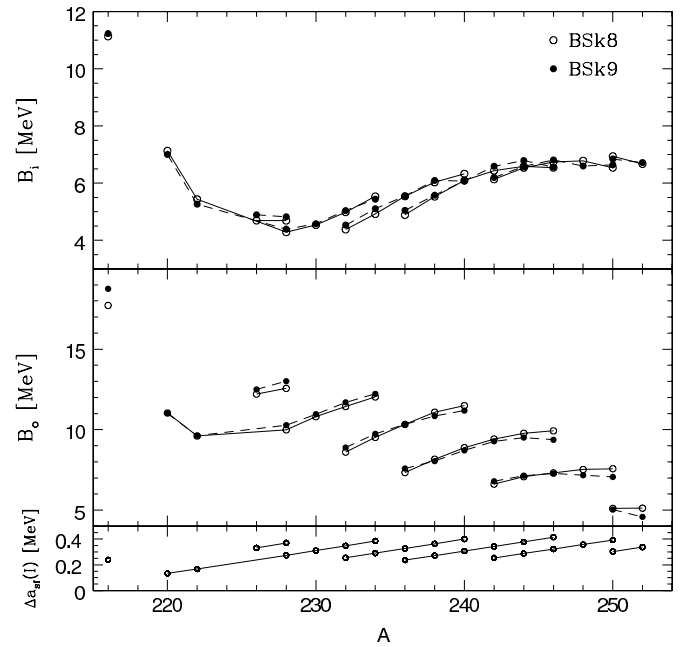
FIG. 13. Inner and outer reflection-symmetric barrier heights of even-even actinides ($Z = 88$–98) with BSk8 ($J = 28$ MeV) and BSk9 ($J = 30$ MeV) within the HFB + PLN framework; the bottom panel gives $\Delta a_{sf}(I) = a_{sf}(I, \text{BSk8}) - a_{sf}(I, \text{BSk9})$, the difference between the effective surface-energy coefficients of both forces for all nuclei considered.

pairing leading to lower barriers (Sec. III A) is opposed by the reduction of the effective mass, which alone would lead to higher barriers. It seems that the essentially exact compensation between the shift in the effective mass and the shift in pairing that we have achieved in forces BSk2 and BSk6 for the masses holds equally well for the fission barriers of the nuclei considered here.

E. Comparison of BSk6 and BSk7: Role of density dependence of pairing

Our forces BSk6 and BSk7 differ only in that the pairing term of the latter is density dependent; the parameter η

TABLE VII. Primary fission barriers of some neutron-rich nuclei calculated with forces BSk1, BSk2, and BSk6 within the HFB model and BSk8 and BSk9 within the HFB + PLN model. Also given is the prediction with the ETFSI (SkSC4) approximation [16]. Reflection symmetry was assumed for all but the ETFSI calculations (in the latter case the asymmetry parameter $\tilde{\alpha}$ is given if not zero); (i) and (o) refer to inner and outer barriers, respectively. The same rotational correction (12) is used for all but the ETFSI calculations.

Z	N	A	BSk1	BSk2	BSk6	BSk8	BSk9	ETFSI
84	170	254	25.4	25.8	23.7	28.3 (o)	24.4 (o)	26.9 ($o^{\tilde{\alpha}=.45}$)
84	184	268	36.4	28.6	31.4	37.1 (o)	33.1 (o)	39.0 (o)
92	170	262	10.5	9.9	8.5	11.5 (o)	9.6 (o)	5.3 ($o^{\tilde{\alpha}=.47}$)
92	184	276	18.0	9.9	12.2	16.8 (o)	15.0 (o)	17.7 (o)
92	194	286	12.4	10.6	10.0	15.4 (o)	10.0 (o)	10.9 (o)
100	170	270	3.8	3.0	2.9	4.2 (o)	3.7 (o)	2.2 (i)
100	184	284	6.2	2.1	3.1	5.3 (o)	5.1 (o)	6.0 (i)
100	194	294	2.6	2.2	2.3	3.2 (o)	2.3 (o)	1.6 (i)
100	210	310	6.2	4.2	4.2	6.4 (o)	4.8 (i)	7.3 (i)
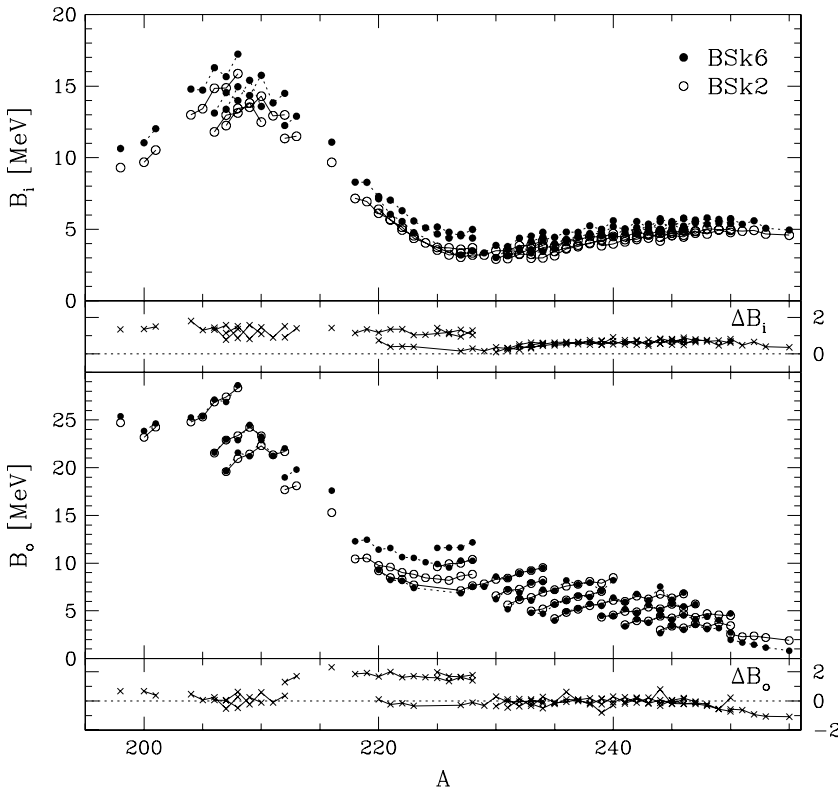
FIG. 14. HFBCS (BSk6) inner and outer barrier heights compared to those of HFBCS (BSk2); $\Delta B_{i,o} = B_{i,o}$ (BSk6) $-B_{i,o}$ (BSk2).

appearing in Eq. (2) takes the value 0.45 for the latter and 0 for the former. Otherwise the two forces have been fitted under identical conditions to the mass data, and the rms deviations turn out to be almost identical. However, although there is nothing in the mass data requiring such a density dependence, we do know that the mass data rule out any stronger density dependence (i.e., any higher value of η [5,6]). In particular, a pure surface pairing, corresponding to $\eta = 1$, gives much too high an rms deviation. Here we report on barrier calculations for these two forces, performed with a view to seeing whether fission data can be more informative than the mass data on the question of a possible density dependence in the pairing force.

The BSk6 and BSk7 barrier heights are shown in Fig. 15 for the 114 inner and outer barrier heights of nuclei for which one or both barrier heights are known. It is seen that the barriers are essentially the same for the two forces, which means that fission cannot tell us anything about a possible density dependence of the pairing force that we did not know already from masses.

F. Comparison of BSk1 and BSk2: Role of pairing cutoff

The only imposed difference between BSk1 and BSk2 lies in the definition of the pairing cutoff: The BSk1 pairing is characterized by an energy cutoff of $\hbar\omega$ into the continuum, whereas BSk2 only allows pairing to act within 15 MeV of the Fermi energy. The latter choice of pairing cutoff has been shown to be crucial for the mass fit of the post-1995 data [4], which means that although the BSk1 mass fit was optimized within the constraint of the imposed pairing cutoff,

it is definitely not equivalent to the BSk2 fit, the latter being of significantly higher quality. Figure 16 shows that the change of cutoff prescription has implications for fission barriers as well; the BSk2 barriers lie generally about 1 MeV lower than those of BSk1.
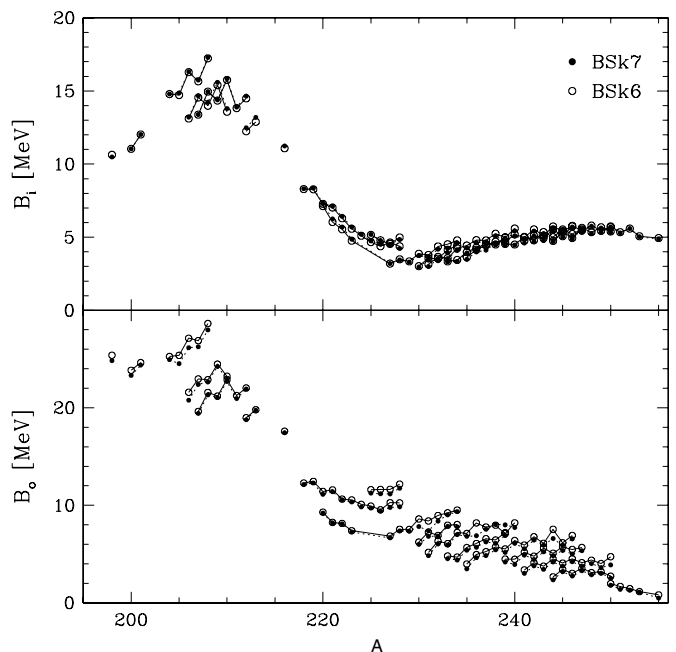
FIG. 15. Comparison of inner and outer BSk6 and BSk7 barrier heights calculated in the HFBCS approximation. The two Skyrme forces differ in the density dependence of the pairing interaction.
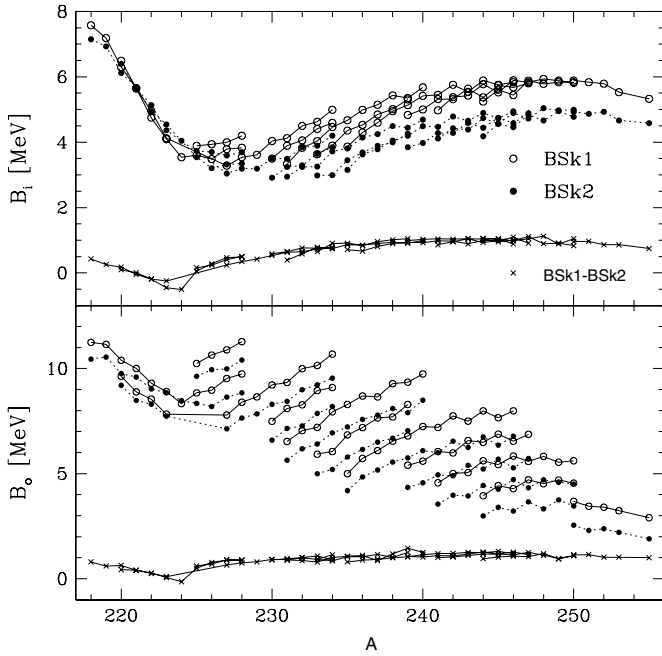
FIG. 16. Inner and outer barrier heights obtained with BSk1 and BSk2 Skyrme forces that differ only in the cutoff prescription: $\hbar\omega$ for the former and $\epsilon_F + 15$ MeV for the latter.

These results can be understood by analyzing the phase space above the Fermi energy, which for heavy nuclei close to the stability line lies typically at about -6 MeV for both neutrons and protons. Thus for BSk2 sp levels are included up to about 9 MeV, whereas for BSk1 the sp spectrum goes up only to 6 or 7 MeV, with $\hbar\omega$ falling in this range for these nuclei. Both forces have been normalized to the ground-state energy through the mass fit, but the pairing energy at the saddle point will be larger for BSk2 than for BSk1, because the sp level density is higher there than at the ground state. As a result, BSk2 barriers are lower than those for BSk1. This same argument leads us to expect that as we move away from the stability line the BSk2 barriers will become still lower relative to those given by BSk1.

VI. FISSION BARRIERS FAR FROM STABILITY

Probably the most striking feature of the ETFSI barrier calculations of highly neutron rich nuclei [16] is the very high primary barriers predicted in the region of the $N = 184$ magic number, a result that has a considerable impact on r-process calculations. In this section we investigate the extent to which this conclusion holds up in HFB calculations, reporting calculations that we have made on a few selected nuclei in this region of the nuclear chart with forces BSk1, BSk2, BSk6, BSk8, and BSk9. Our results are shown in Table VII, along with the original ETFSI results [16] (see also www.astro.ulb.ac.be). Since all but two of the nine primary ETFSI barriers that we show in this table are left-right symmetric we imposed this constraint on these HFB calculations.

The ETFSI calculations [16] were performed with the force SkSC4, for which the pairing cutoff prescription is the same as for the force BSk1, and we see from Table VII that the barrier heights of these exotic nuclei are quite similar for the two sets of calculations (except in the case of ^{262}U). The heights for BSk2 are quite similar to those for BSk1, except that the prescription for the pairing cutoff is much better adapted to the latest mass data, and we have argued at the end of Sec. V F that it should lead to lower barriers in highly neutron rich nuclei. This is confirmed in Table VII, with barriers being lowered by as much as 8 MeV.

However, as we have already discussed, BSk8 and BSk9 are our only forces that are not manifestly incompatible with the barrier data, and for BSk8 the barriers of the neutron-rich nuclei shown in Table VII are much higher than those for BSk2. To understand this result, it is convenient to consider the intermediate case of BSk6, which shows substantial differences from BSk2, particularly in the vicinity of the $N = 184$ magic number. It seems that the almost exact compensation that takes place between the shift in M_s^* and that of the pairing for barriers of nuclei lying fairly close to the stability line (see Sec. V D) no longer holds far from stability. However, the relationship between the BSk6 and BSk8 barriers for these neutron-rich nuclei is exactly as discussed for nuclei closer to stability in Sec. V B: The higher value of a_{sf}^0 leads to the higher barriers of BSk8. We see that the ETFSI prediction of very high barriers at $N = 184$ is upheld by the HFB + PLN calculation with BSk8.

For BSk9, with its higher J value, there is a significant lowering of barriers, the extreme case being ^{268}Po, for which the barrier is 6 MeV lower than with ETFSI ($J = 27.5$ MeV for the force SkSC4 of the ETFSI calculations). Nevertheless, the BSk9 barriers will be closer to the ETFSI barriers than to those of the compilation of Howard and Möller [13].

VII. CONCLUSIONS

We have performed constrained Skyrme-Hartree-Fock-Bogoliubov calculations of the fission barriers of a large number of nuclei for which data exist. Our code restores broken symmetries such as translational invariance, particle-number conservation, parity, and, in a more approximate way, rotational invariance. Axial symmetry is imposed, but reflection asymmetry is allowed. Tondeur's flooding algorithm is used to locate the fission path in the three-dimensional space spanned by the constrained degrees of freedom. The principal interaction used is BSk8, the force on which the HFB-8 mass table is based [7].

For nuclei with $92 \leqslant Z \leqslant 98$ the agreement of our calculations with the measured primary barriers is excellent, with an rms deviation of 0.722 MeV, which is a significant improvement on the semiclassical ETFSI calculations [15]. For lighter nuclei, however, the calculated primary barriers are always too high because of the existence of a third barrier at very high deformations that is not influenced by the reflection asymmetry. However, our calculated superheavy barriers appear to be too low, although we stress the somewhat tenuous nature of the data in this region. The origin of

these deviations between our calculated barriers and the experimental data lies most probably with the choice of the force. It is clear that the excellent fit to the mass data given by this force is not a sufficient condition to guarantee good fission barriers from the Pb to the superheavy region.

With a view to seeing what changes should be made to the force to improve the calculated barriers while maintaining the quality of the mass fit, we have made comparative tests with other Skyrme forces.

ACKNOWLEDGMENTS

APPENDIX A: EXTRACTION OF SURFACE-STIFFNESS COEFFICIENT Q FROM CALCULATIONS OF SEMI-INFINITE NUCLEAR MATTER

We have used at various times each of three methods for extracting the surface-stiffness coefficient Q from calculations of SINM, with the result that we have given different results in different papers for the same force. Here we try to regularize the situation, once and for all. The respective methods are based on the following droplet-model properties of SINM:

(i) The surface energy per unit area is given by Eqs. (4.46) and (4.46b) of Ref. [28] as

$$\sigma(I) = \frac{1}{4\pi\, r_0^2}\left(a_{\rm sf}^0 + \frac{9J^2}{4Q}I^2\right), \qquad \text{(A1)}$$

where I represents here the limiting fractional neutron excess, $(\rho_n - \rho_p)_c/(\rho_n + \rho_p)_c$, deep below the surface of the system.

(ii) The neutron-skin thickness θ_n of SINM is given by Eq. (2.21) of Ref. [28] as

$$\theta_n(I) = \frac{3J}{2Q}r_0 I. \qquad \text{(A2)}$$

(iii) The variation of σ with the limiting density $(\rho_n + \rho_p)_c$ is given by Eq. (3.34) of [65] as

$$\dot{\sigma} = \frac{r_0 J^2}{Q}I^2. \qquad \text{(A3)}$$

In Table VIII we show the results that we have obtained for Q using each of these three methods, labeled σ, θ_n, and $\dot{\sigma}$, respectively; the parameter set is BSk8. In principle, our results should be independent of the value of I taken in our calculations, but we see that this is far from the case, presumably because of numerical errors and higher order terms in I that should have been included in these expressions. (A similar pattern is found for all the other forces.) Nevertheless, the θ_n method is far more stable than the other two methods, the variation with I being slow and close to linear. This, therefore, is the method that we adopted in Table II for all forces; the

TABLE VIII. Calculation by three different methods (see text) of surface-stiffness coefficient Q (in MeV) for force BSk8, as a function of limiting fractional neutron excess I.

I^2	σ	θ_n	$\dot{\sigma}$
0.01	29.9	44.9	49.3
0.02	37.5	44.2	52.4
0.03	41.5	43.7	52.8
0.04	43.7	43.1	52.5
0.05	45.0	42.5	51.9

computed values of Q are in all cases extrapolated down to $I = 0$.

APPENDIX B: PARITY-SYMMETRY RESTORATION

The mass asymmetry of fission fragment distributions is due to the energetically favored pear shape of the nuclear density at the outer saddle point down to the scission point. The corresponding degree of freedom, the reflection asymmetry, is added to the wave function $|\Psi\rangle$ at the cost of symmetry breaking: The single-particle HF orbitals have lost their definite parity during solution of the Schrödinger equation, which contradicts the relation $[H, \Pi] = 0$, where H is the Hamiltonian and Π is the parity operator. In other words, the pear shape of the density of such a nucleus found in the intrinsic system of coordinates is unphysical: The exact wave function has a good parity quantum number (i.e., left-right asymmetry is not privileged with respect to right-left asymmetry); the wave functions of both configurations are degenerate in energy. To describe the reflection asymmetry coherently, we restore the parity symmetry on the basis of the generator coordinate method (GCM), extensively described in [66].

To recover a wave function of definite parity, the projector

$$P^\pi = \tfrac{1}{2}(1 + \pi\,\Pi), \qquad \text{(B1)}$$

where $\pi = \pm 1$ are the eigenvalues of Π, is applied on the reflection symmetry breaking wave function $|\Psi\rangle$. The normalized expectation value of the Hamiltonian in the projected state $|\Psi^\pi\rangle = P^\pi|\Psi\rangle$ reads

$$E^\pi = \frac{\langle\Psi^\pi|H|\Psi^\pi\rangle}{\langle\Psi^\pi|\Psi^\pi\rangle} \qquad \text{(B2)}$$

$$= \frac{\langle\Psi|H P^\pi|\Psi\rangle}{\langle\Psi|P^\pi|\Psi\rangle} \qquad \text{(B3)}$$

$$= \frac{\langle\Psi|H|\Psi\rangle + \pi\langle\Psi|H\Pi|\Psi\rangle}{\langle\Psi|\Psi\rangle + \pi\langle\Psi|\Pi|\Psi\rangle}, \qquad \text{(B4)}$$

where the parity of H, $[H, P^\pi] = 0$, has been used. The contribution to the projected energy, $E_\Pi = \langle\Psi|H\Pi|\Psi\rangle/\langle\Psi|\Pi|\Psi\rangle$, may be written in the familiar form as a space integral of the local energy density: in the p-h channel,

$$E_\Pi^{p\text{-}h} = \int \mathcal{E}_\Pi^{p\text{-}h}(\mathbf{r})d^3\mathbf{r}, \qquad \text{(B5)}$$

where $\mathcal{E}_{\Pi}^{p-h}(\mathbf{r})$ is formally identical to Eqs. (3a) and (3b) of [33], whereas in the p-p channel,

$$E_{\Pi}^{p-p} = \sum_{q=n,p} \frac{V_{\pi q}}{4} \int \left[1 - \eta \left(\frac{\rho}{\rho_0} \right)^{\alpha} \right] \tilde{\rho}_q(\mathbf{r}) \tilde{\rho}_q^{*\pi}(\mathbf{r}) d^3\mathbf{r}. \quad \text{(B6)}$$

The densities entering Eqs. (B5) and (B6) must however be redefined as functions of contractions that are given by the GCM formalism [66]. The calculation of the additional matrix elements $\langle \Psi | H \Pi | \Psi \rangle$ and $\langle \Psi | \Pi | \Psi \rangle$ is transformed in a calculation of contractions. The advantage of implementing such a technique is that it can be used for other projections, such as the angular momentum projection, and to study the low-lying spectrum of nuclei.

The contractions $\langle a_k^{\dagger} b_l \rangle$ entering the various (local) densities,

$$\rho(\mathbf{r}) = \sum_{kl} \langle a_k^{\dagger} b_l \rangle \Phi_k^{\dagger}(\mathbf{r}) \Phi_l^{\pi}(\mathbf{r}), \quad \text{(B7)}$$

$$\tau(\mathbf{r}) = \sum_{kl} \langle a_k^{\dagger} b_l \rangle \nabla \Phi_k^{\dagger}(\mathbf{r}) . \nabla \Phi_l^{\pi}(\mathbf{r}), \quad \text{(B8)}$$

$$\mathbf{J}(\mathbf{r}) = -\frac{i}{2} \sum_{kl} \langle a_k^{\dagger} b_l \rangle \{ \Phi_k^{\dagger}(\nabla \times \hat{\boldsymbol{\sigma}}) \Phi_l^{\pi} - [(\nabla \times \hat{\boldsymbol{\sigma}}) \Phi_k^{\dagger}] \Phi_l^{\pi} \}, \quad \text{(B9)}$$

$$\nabla \cdot \mathbf{J}(\mathbf{r}) = \tau(\mathbf{r}) - \sum_{kl} \langle a_k^{\dagger} b_l \rangle (\hat{\boldsymbol{\sigma}} \cdot \nabla \Phi_k^{\dagger})(\hat{\boldsymbol{\sigma}} \cdot \nabla \Phi_l^{\pi}), \quad \text{(B10)}$$

and the contractions $\langle a_k^{\dagger} a_{\bar{l}}^{\dagger} \rangle$ and $\langle b_k b_{\bar{l}} \rangle$ entering the local pair densities [in Eq. (B11), the creation operators act on the left states; in Eq. (B12), annihilation operators act on the right parity-transformed states],

$$\tilde{\rho}_l(\mathbf{r}) = \sum_{kl} \langle a_k^{\dagger} a_{\bar{l}}^{\dagger} \rangle \boldsymbol{\Phi}_k^{\dagger}(\mathbf{r}) \Phi_l(\mathbf{r}), \quad \text{(B11)}$$

$$\tilde{\rho}_{\eta}^{\pi}(\mathbf{r}) = \sum_{kl} \langle b_k b_{\bar{l}} \rangle \boldsymbol{\Phi}_k^{\pi\dagger}(\mathbf{r}) \Phi_l^{\pi}(\mathbf{r}), \quad \text{(B12)}$$

are given in [66] in term of the unitary matrix that relates the parity-transformed HF single-particle states ($b_l^{\dagger} \equiv \phi_l^{\pi} = \Pi \phi_l$) and the HF single-particle states ($a_k^{\dagger} \equiv \phi_k$):

$$a_k = \sum_l R_{kl} b_l. \quad \text{(B13)}$$

Expanding a_k and b_l on an arbitrary basis c_m,

$$a_k = \sum_m D_{km}^* c_m \quad \text{and} \quad b_l = \sum_m E_{lm}^* c_m, \quad \text{(B14)}$$

one obtains

$$R = D^* E^t, \quad \text{(B15)}$$

where the unitarity of E was used. In the case of wave functions developed on an axially deformed oscillator basis, a component of the spinor of the single-particle wave function,

$$\boldsymbol{\Phi}_k(\mathbf{r}) = \begin{pmatrix} \Phi_k^+(\eta, z) e^{im_k^+ \varphi} \\ \Phi_k^-(\eta, z) e^{im_k^- \varphi} \end{pmatrix}, \quad \text{(B16)}$$

transforms under the parity operator Π as

$$\Pi \Phi_k^{\sigma}(\eta, z) e^{im^{\sigma} \varphi} = \frac{1}{\sqrt{2\pi}} e^{im^{\sigma} \varphi}$$
$$\times \sum_{n_{\eta}, n_z} (-)^{n_z + m^{\sigma}} C_{\gamma, m^{\sigma}}^k \psi_{n_{\eta}}^{m^{\sigma}}(\eta) \psi_{n_z}(z), \quad \text{(B17)}$$

where the subscript γ stands for the quantum numbers (n_{η}, n_z), the number of nodes in the r and z directions, respectively. In the case of axial symmetry, the projection of the total angular momentum on the z axis, Ω, is a good quantum number, which allows us to write R_{kl} as a block diagonal matrix:

$$R_{kl}(\Omega) = \sum_{\sigma = \pm \frac{1}{2}} \sum_{\gamma \leqslant \gamma_{\max}} (-)^{n_z + m^{\sigma}} C_{\gamma, m^{\sigma}}^k C_{\gamma, m^{\sigma}}^l. \quad \text{(B18)}$$

In these expressions, $m^{(\sigma)}$ (Λ in [3]) and $\sigma = \pm 1/2$ are the projections on the z axis of the orbital angular momentum and nucleon spin, respectively ($\Omega = m^{(\sigma)} + \sigma$), and $\gamma_{\max} = \gamma_{\max}(m^{(\sigma)})$ is the upper limit of the couple (n_{η}, n_z) that corresponds to the truncation of the deformed oscillator basis states with respect to the cutoff energy $E_{\mathrm{osc}}(n_{\eta}, n_z, |m^{(\sigma)}|)$ [3]. As advised in [66], the dimension N of R can be reduced to $n < N$ if the irrelevant single-particle states with a small occupation probability are neglected; here, the lower limit is taken as $v_k^2 = 10^{-6}$. Therefore, the occupations can be written as block diagonal matrices of the form

$$u = \begin{pmatrix} \bar{u} & 0 \\ 0 & 1 \end{pmatrix}, \quad v = \begin{pmatrix} \bar{v} & 0 \\ 0 & 0 \end{pmatrix}, \quad \text{(B19)}$$

where $\bar{u}$ is an $(n \times n)$ diagonal matrix. Similarly, the unitary matrix R_{kl} can be decomposed as

$$R = \begin{pmatrix} \mathcal{R} & \mathcal{S} \\ \mathcal{T} & \mathcal{U} \end{pmatrix}, \quad \text{(B20)}$$

where $\mathcal{R}$ is an $(n \times n)$ unitary matrix. For completeness, the contractions are given here, in the notation of [66]:

$$\langle a_k^{\dagger} b_l \rangle = \langle a_{\bar{k}}^{\dagger} b_{\bar{l}} \rangle^* = \begin{pmatrix} \bar{v}_g \tilde{\mathcal{D}} \bar{v}_d & 0 \\ 0 & 0 \end{pmatrix}, \quad \text{(B21)}$$

$$\langle a_k^{\dagger} a_{\bar{l}}^{\dagger} \rangle = -\langle a_{\bar{k}}^{\dagger} a_l^{\dagger} \rangle^* = \begin{pmatrix} \bar{u}_g \bar{v}_g - \bar{v}_g \mathcal{E}_g^* \mathcal{D}^* \bar{v}_g & 0 \\ 0 & 0 \end{pmatrix}, \quad \text{(B22)}$$

$$\langle b_k b_{\bar{l}} \rangle = -\langle b_{\bar{k}} b_l \rangle^* = \begin{pmatrix} -\bar{u}_d \bar{v}_d - \bar{v}_d \mathcal{D} \mathcal{E}_d \bar{v}_d & 0 \\ 0 & 0 \end{pmatrix}, \quad \text{(B23)}$$

with

$$\mathcal{D} = (\bar{u}_g (\mathcal{R}^{\dagger})^{-1} \bar{u}_d + \bar{v}_g \mathcal{R} \bar{v}_d)^{-1}, \quad \text{(B24)}$$

$$\mathcal{E}_g = (\bar{u}_g \mathcal{R} \bar{v}_d - \bar{v}_g (\mathcal{R}^{\dagger})^{-1} \bar{u}_d), \quad \text{(B25)}$$

$$\mathcal{E}_d = (\bar{u}_g (\mathcal{R}^{\dagger})^{-1} \bar{v}_d - \bar{v}_g \mathcal{R} \bar{u}_d), \quad \text{(B26)}$$

and, if the dimension of both left and right matrices is equal,

$$\langle L | R \rangle = \langle \Psi | \Pi | \Psi \rangle = \left| \frac{\det \mathcal{R}}{\det \mathcal{D}} \right|. \quad \text{(B27)}$$

In the present problem, the non-negligible occupation probabilities $\bar{v}^2$ of the left state, $\langle L| = \langle \Psi|$, and the right state, $|R\rangle = \Pi|\Psi\rangle$ are equal: $\bar{v}_g = \bar{v}_d$ and $\bar{u}_g = \bar{u}_d$.

We note that when the restoration of both parity and particle number symmetries are required (for the BSk8 force), they are performed separately (i.e., not according to Ref. [67]): The parity projection energy, calculated using the particle-number-unprojected HFB state, is subtracted from the total internal energy obtained with the particle-number-projected HFB + PLN state.

---

[1] B. Meyer, Annu. Rev. Astron. Astrophys. **32**, 153 (1994).

[2] M. Arnould and K. Takahashi, Rep. Prog. Phys. **62**, 395 (1999).

[3] M. Samyn, S. Goriely, P.-H. Heenen, J. M. Pearson, and F. Tondeur, Nucl. Phys. **A700**, 142 (2002).

[4] S. Goriely, M. Samyn, P.-H. Heenen, J. M. Pearson, and F. Tondeur, Phys. Rev. C **66**, 024326 (2002).

[5] M. Samyn, S. Goriely, and J. M. Pearson, Nucl. Phys. **A725**, 69 (2003).

[6] S. Goriely, M. Samyn, M. Bender, and J. M. Pearson, Phys. Rev. C **68**, 054325 (2003).

[7] M. Samyn, S. Goriely, M. Bender, and J. M. Pearson, Phys. Rev. C **70**, 044309 (2004).

[8] S. Goriely, M. Samyn, J. M. Pearson, and M. Onsi, Nucl. Phys. **A750**, 425 (2005).

[9] G. Audi and A. Wapstra, Nucl. Phys. **A595**, 409 (1995).

[10] G. Audi, A. Wapstra, and C. Thibault, Nucl. Phys. **A729**, 3 (2003).

[11] L. Bonneau, P. Quentin, and D. Samsoen, Eur. Phys. J. A **21**, 391 (2004).

[12] T. Bürvenich, M. Bender, J. Maruhn, and P.-G. Reinhard, Phys. Rev. C. **69**, 029901(E) (2004).

[13] W. Howard and P. Möller, At. Data Nucl. Data Tables **25**, 219 (1980).

[14] P. Möller, A. J. Sierk, and A. Iwamoto, Phys. Rev. Lett. **92**, 072501 (2004).

[15] A. Mamdouh, J. M. Pearson, M. Rayet, and F. Tondeur, Nucl. Phys. **A644**, 389 (1998).

[16] A. Mamdouh, J. M. Pearson, M. Rayet, and F. Tondeur, Nucl. Phys. **A679**, 337 (2001).

[17] A. Dutta, J.-P. Arcoragi, J. M. Pearson, R. Behrman, and F. Tondeur, Nucl. Phys. **A458**, 77 (1986).

[18] F. Tondeur, A. Dutta, J. M. Pearson, and R. Behrman, Nucl. Phys. **A470**, 93 (1987).

[19] J. M. Pearson, Y. Aboussir, A. K. Dutta, R. C. Nayak, M. Farine, and F. Tondeur, Nucl. Phys. **A528**, 1 (1991).

[20] Y. Aboussir, J. M. Pearson, A. Dutta, and F. Tondeur, Nucl. Phys. **A549**, 155 (1992).

[21] Y. Aboussir, J. M. Pearson, A. Dutta, and F. Tondeur, At. Data Nucl. Data Tables **61**, 127 (1995).

[22] W. D. Myers and W. J. Swiatecki, Phys. Rev. C **60**, 014606 (1999).

[23] W. Myers and W. Swiatecki, Nucl. Phys. **A601**, 141 (1996).

[24] M. Bender, G. F. Bertsch, and P.-H. Heenen, Phys. Rev. C **69**, 034340 (2004).

[25] E. Chabanat, P. Bonche, P. Haensel, J. Meyer, and R. Schaeffer, Nucl. Phys. **A635**, 231 (1998); [Erratum: *ibid*. **A643**, 441(E) (1998)].

[26] M. Bender, Ph.D. thesis, Johan Wolfgang Goethe-Universität in Frankfurt am Main, 1997.

[27] M. Kutschera and W. Wójcik, Phys. Lett. **B325**, 271 (1994).

[28] W. D. Myers and W. J. Swiatecki, Ann. Phys. (NY) **55**, 395 (1969).

[29] D. Vautherin, Phys. Rev. C **7**, 296 (1973).

[30] A. K. Dutta, J. M. Pearson, and F. Tondeur, Phys. Rev. C **61**, 054303 (2000).

[31] P. Ring and P. Schuck, *The Nuclear Many-Body Problem* (Springer, Berlin, 1980).

[32] M. Bender, P.-H. Heenen, and P.-G. Reinhard, Rev. Mod. Phys. **75**, 121 (2003).

[33] F. Tondeur, S. Goriely, J. M. Pearson, and M. Onsi, Phys. Rev. C **62**, 024308 (2000).

[34] M. Butler, D. Sprung, and J. Martorell, Nucl. Phys. **A422**, 157 (1984).

[35] D. Vautherin and D. Brink, Phys. Rev. C **5**, 626 (1972).

[36] D. Inglis, Phys. Rev. **96**, 1059 (1954).

[37] D. Inglis, Phys. Rev. **103**, 1786 (1956).

[38] S. Belyaev, Nucl. Phys. **24**, 322 (1961).

[39] S. Goriely, F. Tondeur, and J. M. Pearson, At. Data Nucl. Data Tables **77**, 311 (2001).

[40] J. Skalski, P.-H. Heenen, P. Bonche, H. Flocard, and J. Meyer, Nucl. Phys. **A551**, 109 (1993).

[41] B. Giraud, J. LeTourneux, and S. Wong, Phys. Lett. **B32**, 23 (1970).

[42] H. Flocard, P. Quentin, A. Kerman, and D. Vautherin, Nucl. Phys. **A203**, 433 (1973).

[43] M. Brack, J. Damgaard, A. Jensen, H. Pauli, V. Strutinsky, and C. Wong, Rev. Mod. Phys. **44**, 320 (1972).

[44] S. Raman, C. H. Malarkey, W. T. Milner, C. W. J. Nestor, and P. H. Stelson, At. Data Nucl. Data Tables **36**, 1 (1987).

[45] F. Tondeur (private communication).

[46] J. C. Maxwell, London, Edinburgh, Dublin Philos. Mag. J. Sci. **40**, 421 (1870).

[47] A. Cayley, London, Edinburgh, Dublin Philos. Mag. J. Sci. **18**, 264 (1859).

[48] Reference Input Parameter Library—2, IAEA, Vienna (2002), tecDoc (2003), unpublished; also available at www-nds.iaea.org.

[49] M. Hunyadi, D. Gassmann, A. Krasznahorkay, D. Habs, P. Thirolf, M. Csatlós, Y. Eisermann, T. Faestermann, G. Graw, J. Gulyás *et al.*, Phys. Lett. **B505**, 27 (2001).

[50] W. Stepien and Z. Szymanski, Phys. Lett. **B26**, 181 (1968).

[51] H. Flocard, P. Quentin, D. Vautherin, M. Vénéroni, and A. Kerman, Nucl. Phys. **A231**, 176 (1974).

[52] K. Rutz, M. Bender, P. G. Reinhard, and J. A. Maruhn, Phys. Lett. **B468**, 1 (1999).

[53] S. Hofmann and G. Münzenberg, Rev. Mod. Phys. **72**, 733 (2000).

[54] G. Audi and A. Wapstra (private communication).

[55] J. Blons, B. Fabbro, C. Mazur, D. Paya, and M. Ribrag, Nucl. Phys. **A477**, 231 (1988).

[56] A. Grewe, S. Andriamonje, C. Böckstiegel, T. Brohm, H.-G. Clerc, S. Czajkowski, E. Hanelt, A. Heinz, M. Itkis, M. de Jong *et al.*, Nucl. Phys. **A614**, 400 (1997).

[57] G. N. Smirenkin, Report INDC(CCP)-359, 1993 (unpublished); also available at www-nds.iaea.org/ripl/.

[58] J. Lynn, Tech. Rep., U. K. Atomic Energy Authority, 1974 (unpublished).

[59] M. Samyn, S. Goriely, and J. M. Pearson, *Realistic fission barrier calculations within the Skyrme Hartree-Fock theory, Proceedings of the Third International Conference on Fission and properties of neutron-rich nuclei, Sanibel Island, Florida, USA 3–9 November 2002*, edited by A. V. Ramayya and H. K. Carter (World Scientific, Singapore, 2003), p. 679.

[60] H. Goutte, J. F. Berger, P. Casoli, and D. Gogny, Phys. Rev. C **71**, 024316 (2005).

[61] M. G. Itkis, Y. T. Oganessian, and V. I. Zagrebaev, Phys. Rev. C **65**, 044602 (2002).

[62] W. Myers and W. Swiatecki, Nucl. Phys. **81**, 1 (1966).

[63] S. Ćwiok, J. Dobaczewski, P.-H. Heenen, P. Magierski, and W. Nazarewicz, Nucl. Phys. **A611**, 211 (1996).

[64] J. Bartel, P. Quentin, M. Brack, C. Guet, and H.-B. Håkansson, Nucl. Phys. **A386**, 79 (1982).

[65] M. Farine and J. M. Pearson, Nucl. Phys. **A422**, 1 (1984).

[66] P. Bonche, J. Dobaczewski, H. Flocard, P.-H. Heenen, and J. Meyer, Nucl. Phys. **A510**, 466 (1990).

[67] P.-H. Heenen, P. Bonche, J. Dobaczewski, and H. Flocard, Nucl. Phys. **A561**, 367 (1993).